WIND TUNNEL STUDY OF WIND FARMS WITH ALTERNATING 2- AND 3-BLADED WIND TURBINES

BY

IMRAN HAYAT

THESIS

Submitted in partial fulfillment of the requirements
for the degree of Master of Science in Aerospace Engineering
in the Graduate College of the
University of Illinois at Urbana-Champaign, 2017

Urbana, Illinois

Adviser:

Assistant Professor Leonardo P. Chamorro

Abstract

With offshore wind farms gaining substantial momentum in recent years, 2-bladed turbines (2BT) are increasingly becoming a viable alternative to 3-bladed counterparts (3BT). In this wind tunnel study, model wind farms with alternating rows of 3BT and 2BT were explored for potential benefits associated with enhanced momentum available within the arrays and reduced costs due to the reduction of blades. Two arrays of aligned turbines with streamwise separation of five and ten rotor diameter d ($S_x = \Delta x/d$ =5 and 10) were operated in a turbulent boundary layer flow. They shared the same transverse turbine spacing of $S_y = \Delta y/d$ =2.5. High-resolution velocity measurements were made with hotwire anemometry at various locations in the wake and the power output of turbines was measured simultaneously. Comparison of the flow between an array with only 3BT and that with alternating 2BT and 3BT shows enhanced mean velocity and reduced turbulence levels for the latter in $S_x = 5$ case. The pre-multiplied spectra of the flow at selected locations within the wind farm suggest that large energetic structures at top-tip and hub height are dampened by 2BT, with the potential to reduce turbulent loading on downwind turbines. Although the reduced mixing at top-tip height behind 2BT causes the momentum recovery rate to diminish, the available momentum at downstream turbine is still higher than corresponding 3BT in the $S_x = 5$ case. Overall performance gain from marginally enhanced power statistics of 3BT operating in the wake of 2BT is offset by the diminished performance of 2BT inside the farm, resulting in comparable performance between the two configurations.

To

My parents, for their unending love and support

&

AG, for always being there for me.

Acknowledgements

I would like to express my heartfelt gratitude to my advisor Assistant Professor Leonardo P. Chamorro for his dedicated guidance, not only for this thesis but also in shaping my thoughts about my career path. The current work was made possible only through his insight, experience and passion for the subject. I am thankful to my colleagues at Renewable Energy and Turbulent Environment group for providing an atmosphere of learning through their dedication for the subject. I would especially like to thank Huiwen Liu who was instrumental in the experimentation phase. Boshen Liu and Yaqing Jin provided meaningful help in familiarization with the instruments.

I would also like to thank Professor Philippe Geubelle for his support and guidance in the initial phase of MS, which played a vital role in helping me discover my area of interest. Finally, I want to acknowledge the Fulbright Foreign Student program for supporting my graduate studies and research in the US.

Table of Contents

List of Figures

Nomenclature

δ	Boundary layer thickness
λ	Tip-speed ratio
Λ	Integral length scale
ν	Kinematic viscosity of air
ω	Angular velocity of rotor
Φ_u	Spectral density of streamwise velocity fluctuations
Φ_p	Spectral density of power fluctuations
σ_u	Standard deviation of the streamwise velocity fluctuations
$\mathscr{T}$	Integral Time scale
$2BT$	Two-bladed turbine
$3BT$	Three-bladed turbine
C_P	Turbine Power coefficient
C_T	Turbine Thrust coefficient
d	Rotor diameter
I	Turbulence intensity
I_p	Intensity of power fluctuations
$I_{p,farm}$	Overall power fluctuation intensity of the wind farm
$\overline{P}$	Mean power output
Re	Reynolds number
S_x	Streamwise spacing between consecutive turbines normalized by diameter

S_y	Spanwise spacing between adjacent turbines normalized by diameter
T	Turbine Thrust
U	Time-averaged velocity component in streamwise direction
U_{hub}	Incoming velocity at the hub-height of the first row
u'	Streamwise velocity fluctuations
u_*	Friction velocity
z_o	Aerodynamic roughness length
z_{hub}	Hub-height

Chapter 1

Introduction

Numerous countries have set goals for significant contribution from wind energy (17-35%) to their energy portfolio in a medium-term future [1–3]. A recent global renewable energy roadmap [4] estimates that more than 30% of the total energy conversion will be from onshore and offshore wind energies. Notably, the effective surface area covered by the wind farms is estimated to be substantially greater than that of other renewable energy sources. These trends make the problem of wind farm efficiency in terms of power output and spacing, highly relevant in the current scenario.

1.1 Optimization studies

Wind farm optimization has been approached from various angles, owing to its multidisciplinary nature. One popular approach is to apply advanced optimization algorithms to wind turbine spacing and layout to minimize the cost [5, 6] and maximize the power [7]. Chowdhury *et al*. [8] carried out a comprehensive optimization study involving various parameters namely layout, rotor diameter, number of turbines, farm land area and performed a cost analysis per Kilowatt of power produced. Their results were were validated against scaled wind farm wind tunnel experiments. They showed that, in addition to layout optimization, the use of non-identical wind turbines may substantially improve the wind farm power output. Various computational and experimental investigations have been carried out with regard to wind farm power optimization. Yang *et al*. [9] numerically investigated the effect of streamwise and spanwise spacing on power output and found the former to be

more effective in improving power efficiency of turbines. Using Large Eddy Simulations (LES) [10], Meyers & Meneveau [11] estimated an optimal turbine spacing with respect to land area and turbine costs, and found it to be significantly larger than conventionally used spacing. Chamorro *et al*. [12] analyzed a staggered wind farm for different flow characteristics through wind tunnel experiments and showed that the overall power output of a staggered wind farm is about 10% greater than an aligned counterpart.

Another effective, yet less frequently used approach to wind farm power optimization problem is to manipulate the energy extracted from the flow by the upwind turbines to improve the performance of downwind ones. Chamorro *et al*. [13] performed wind tunnel experiments on a model wind farm to investigate wind turbine size heterogeneity as a means to harness the available momentum in the flow more efficiently. The variable rotor diameter and hub-height were reported to have a positive effect on turbulent loading of wind turbines. Adaramola & Krogstad [14] studied the performance of a downwind turbine as a function of yaw angle and tip-speed ratio of the upwind turbine, while noting the effect on overall wind farm efficiency. They showed that by operating the upwind turbine at non-optimal tip-speed ratio and yaw angle, the power output of the downwind turbine is increased such that a significant improvement in the combined total power output of the two turbines is achieved. Conversely, they demonstrated that the same technique can be used to reduce wind turbine spacing, while achieving comparable farm efficiency. A similar study was performed previously by Corten *et al*. [15] in which they concluded that by operating the upwind turbines below optimum power coefficient, not only the net farm power increased but the overall axial loading on turbines also decreased by about 20%. The current study follows the aforementioned line of approach for wind farm power optimization by introducing alternate rows of 2-bladed turbines between 3-bladed turbine rows. In addition to the effect of more energetic wake, the 2-bladed turbines have been shown to have lower energy costs than 3-bladed turbines when operating at higher tip-speed ratios [16]. Furthermore, feasibility of operation of 2-bladed turbines at higher tip-speeds allows a reduction

in torque for given power, leading to lighter and thus cost-effective transmission [17]. All these factors are expected to further enhance power output and economic viability of a hybrid farm composed of 2-bladed and 3-bladed turbines.

1.2 Two-bladed turbine studies

Previous studies on 2-bladed wind turbines have primarily focused on the performance and wake characteristics of individual turbines [18, 19] and turbines within a farm composed of all 2-bladed turbines [20]. Muhle *et al*. [18] compared the wake of a 3-bladed turbine with two 2-bladed ones: one with the same solidity and the other with the same blade aspect-ratio as 3-bladed rotor, all operating at maximum power coefficient C_P. Minor differences in mean velocities were observed especially in the far wake, but the turbulence intensity was found to be higher for the 2-bladed rotors. Medici & Davide [19] reported a faster wake recovery in the central region behind 3-bladed rotors as compared with 2-bladed rotors, although with a greater wake expansion, when both are operating at the same thrust coefficient C_D. Newman *et al*. [20] carried out a comparative PIV analysis between all 3-bladed and all 2-bladed turbine arrays with aligned configurations operating at identical C_P. They observed that the mean velocity field for the two configurations diverged asymptotically in the near wake; whereas the opposite occurred in the far wake, suggesting that the better momentum recovery behind 2-bladed turbines may only be effective in increasing the power output of the first few rows of an array.

1.3 Current work

Despite these efforts on characterizing the power and flow around 2-bladed wind turbines, the potential benefits associated to staggering 2-bladed turbines with 3-bladed ones have not been explored. This fundamental experimental study is a step in that direction. To

facilitate a direct comparison with and potential performance improvement of hybrid wind farms over typical 3-bladed wind turbine arrays, all the experiments have been replicated for both configurations at similar flow conditions. This study attempts to provide a better insight into the power dynamics of turbines operating in a hybrid wind farm, and to explore unique flow features and structures inside a farm. The findings of this investigation may also allow a more robust incorporation of blade number as an input parameter in various optimization techniques. The experimental setup is described in Chapter 2; the single turbine wake and performance characteristics are provided in Chapter 3; Chapter 4 details the results and discussion while conclusions are summarized in Chapter 5.

Chapter 2

Experimental Setup

2.1 Wind tunnel

A laboratory experiment was performed in the Eiffel-type boundary-layer wind tunnel at Renewable Energy and Turbulent Environment group of the University of Illinois at Urbana-Champaign, which has a test section approximately 6.1 m long, 0.91 m wide and 0.45 m high. The fully adjustable wind tunnel ceiling allowed the pressure gradient along the test section to be set to nearly zero during the experiments. Detailed description of the wind tunnel can be found in Adrian *et al*. [21].

2.2 Model wind turbines

Various miniature wind-turbine rotors with two and three blades were fabricated from Objet Vero material with 3D-printers at University of Illinois rapid-prototyping laboratory. The geometry of the 3-bladed rotor is based on a reference model turbine from Sandia National Laboratory [22, 23]. Similarly, the 2-bladed rotor was derived from the same reference model, albeit with one less blade. Therefore, the solidity of the 2-bladed rotor is lower than that of 3-bladed counterpart, whereas the aspect ratio and all other blade characteristics are the same. The model turbines have a rotor diameter d = 120 mm, nacelle length d_n = 10 mm and hub height z_{hub} = 125 mm. A Precision Microdrive 112-001 Micro Core 12 mm DC motor, which has a rated power $P_0 \sim 1$ W, was used as the loading system (generator); further details on the model turbine can be found in Tobin *et al*. [24].

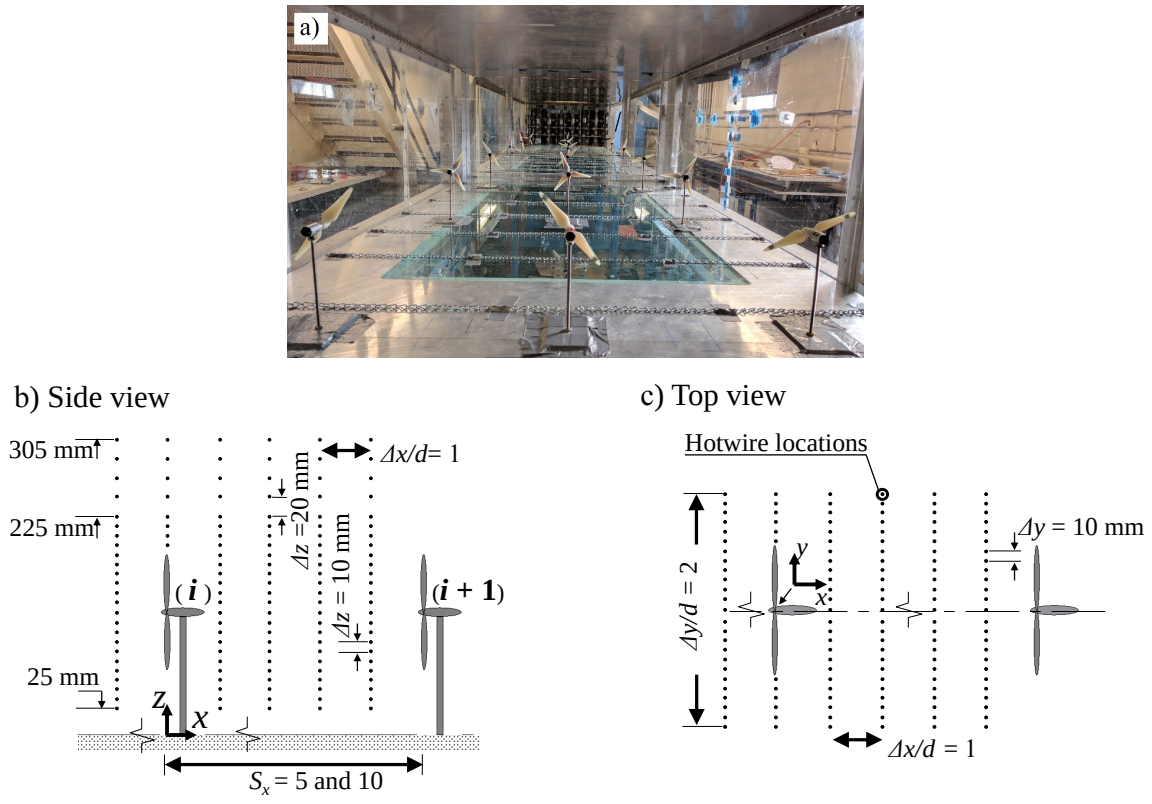

Figure 2.1: a) Photograph of the test section with configuration-A looking upwind; b) detail of the hotwire measurement locations in a vertical plane at the center of middle turbine within representative rows i and $i+1$; c) same as b) but within a wall-parallel plane at hub height.

2.3 Wind farm layouts

Two configurations of model wind farms were tested; the first one (hereon referred to as configuration-A) had alternate rows of 3-bladed and 2-bladed turbines, with 3-bladed ones in the leading row (see Figure 2.1a and Figure 2.2a); whereas the other configuration (hereon configuration-B), was composed of only 3-bladed turbines (see Figure 2.2b). The two wind farm layouts consisted of aligned turbines with streamwise separation of $S_x = \Delta x/d$ = 5 and 10 between adjacent rows, with a common spanwise separation of $S_y = \Delta y/d = 2.5$. This resulted in two arrays of 7×3 and 4×3 turbines for each of the configurations. An additional dummy row was placed downwind of the last turbine row to avoid potential edge effects.

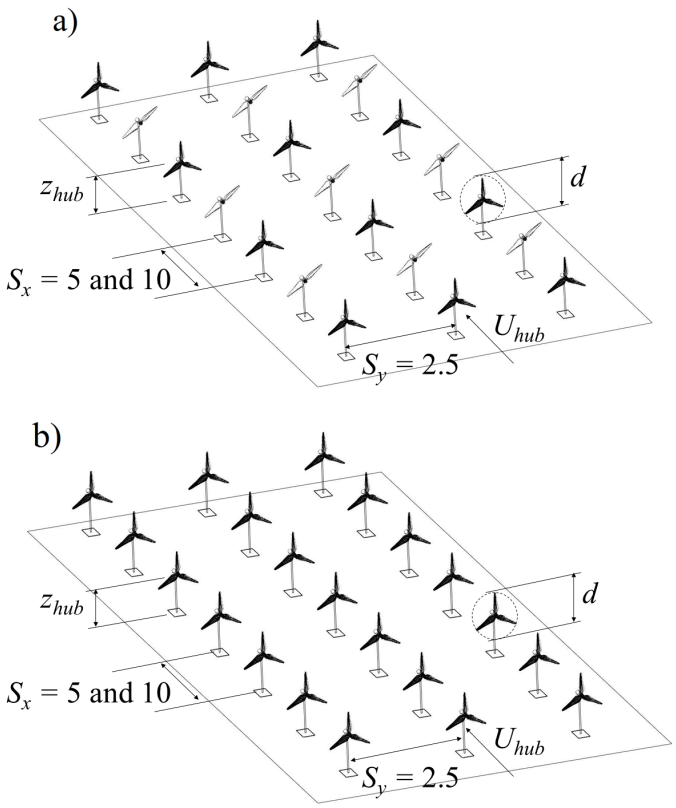

Figure 2.2: Schematics of a) configuration-A with alternating 3- and 2-bladed turbine rows; b) configuration-B with all 3-bladed turbine rows.

2.4 Instrumentation

The streamwise velocity measurements were taken using a high-resolution constant temperature hotwire anemometer, which was calibrated against a pitot static probe in the freestream region of the wind tunnel under minimum background turbulence. Calibrations at the beginning and the end of the experiments ensured that there was negligible voltage offset of the data acquisition system. The probe was moved in the spanwise and vertical directions using a Velmex traversing unit. The hotwire was positioned downwind of each turbine every $\Delta x/d = 1$. At each streamwise location, velocity measurements were made in the central plane ($y = 0$) from z =25 mm to $z = 225$ mm every $\Delta z = 10$ mm and from $z = 225$ mm to $z = 305$ mm every $\Delta z = 20$ mm (Figure 2.1b). Additionally, measurements were also made in the wall-parallel plane at $z = z_{hub}$ for a spanwise range of

$y \in [-120,\ 120]$ mm every $\Delta y = 10$ mm (Figure 2.1c). The hotwire readings were sampled at 10 kHz for measurement periods of 60 s through a Dantec dynamic system. Room temperature of $23 \pm 0.5°$C was maintained throughout the experiments to avoid thermal drift of the voltage signal of hotwire. Instantaneous turbine voltages were measured from the central turbine in each row, at 10 kHz for a period of 120 s using USB-1608HS data acquisition and the power was calculated from the voltage and the terminal resistance (2Ω) of the generator.

2.5 Operating conditions

All the layout cases were operated at an incoming hub-height velocity of approximately $U_{hub} = 9.3$ m s^{-1} resulting in a Reynolds number of $Re = U_{hub}d/\nu \approx 7.31 \times 10^4$, and rotor tip-speed ratio of $\lambda = \omega d/(2U_{hub}) \approx 4.6$ and 5.3 for 3-bladed and 2-bladed turbines respectively, where ν is the kinematic viscosity of air and ω is the angular velocity of the rotor. A high incoming flow turbulence was induced with an active turbulence generator placed at the entrance of the test section (see Figure 2.1a). Each of the horizontal and vertical rods of the turbulence generator was driven separately by a stepper motor at a rotational frequency of 0.1 Hz with random changes in the direction; details of the turbulence generator can be found in Jin *et al*. [25]. The resulting structure of the freestream velocity fluctuations contained a well-developed inertial subrange that spanned two decades. Additionally, the floor along the test section was characterized by roughness elements consisting of approximately 5 mm high chains laid parallel to the spanwise direction every 0.2 m between consecutive chains [26]. The resulting turbulent boundary layer of the incoming flow had a well-defined log region (see Figure 2.3) with a friction velocity of $u_* \approx 0.55$ m s^{-1}, an aerodynamic roughness length of $z_o \approx 0.12$ mm and a thickness of $\delta/z_{hub} \approx 2.2$. Ohya [27] and Chamorro *et al*. [26] used a similar roughness configuration in their wind tunnel experiments to study stable boundary layers and wind turbine wakes over a rough

surfaces. Figure 2.4a,b shows the incoming mean velocity U/U_{hub} and turbulence intensity $I_u = \sigma_u/U_{hub}$ profiles in the central vertical plane, where σ_u denotes the standard deviation of the streamwise velocity fluctuations.

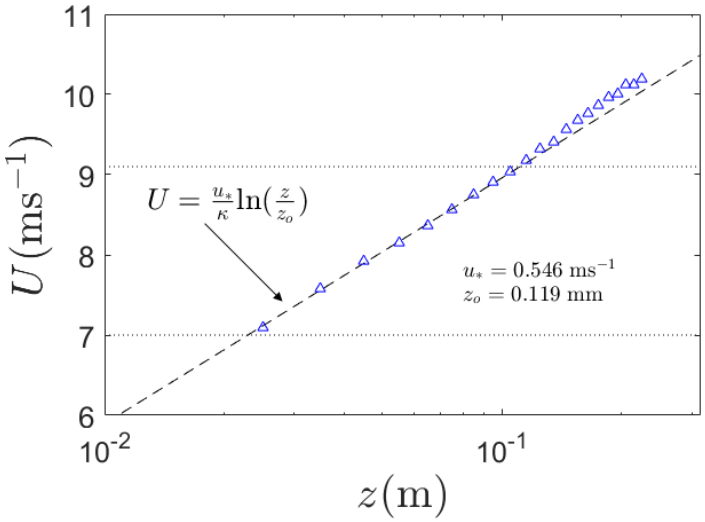

Figure 2.3: Semilog plot of incoming turbulent boundary layer profile showing the log-law region. Triangles represent measured velocity; dashed line represents the log-law fitted to the measurements within the bounds shown by horizontal dotted lines. $\kappa = 0.41$ is the von Karman constant.

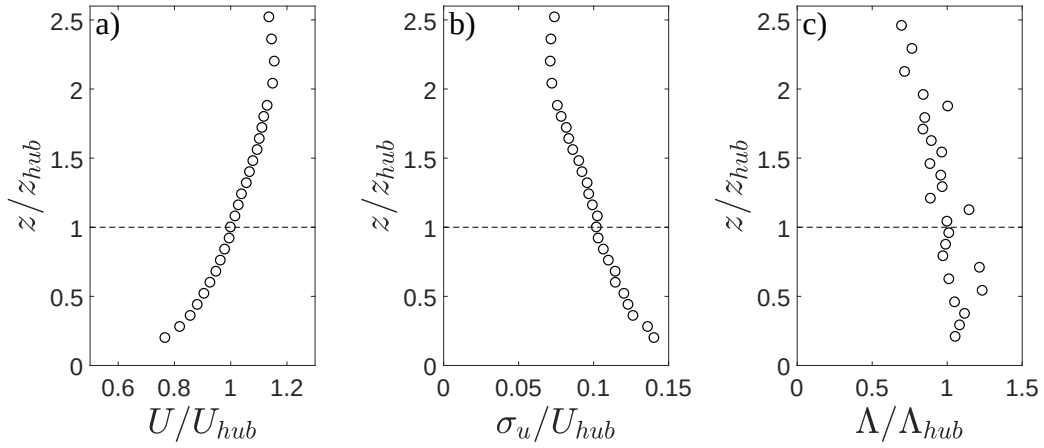

Figure 2.4: Characteristics of the incoming turbulent boundary layer. a) Normalized mean velocity U/U_{hub}; b) turbulence intensity σ_u/U_{hub}, and c) normalized integral length scale $\Lambda^u/\Lambda^u_{hub}$. The horizontal lines represent the turbine axis. Height is normalized with hub height.

Chapter 3

Single Turbine Characterization

In this chapter, we characterize the power performance of the single 3-bladed and 2-bladed turbines operating in free-stream conditions. The wake characteristics of the two types of turbines are also investigated in turbulent boundary layer flow with same operating conditions as that for wind turbine arrays described in Section 2.5.

To characterize the power, representative turbines with two and three blades were placed at mid height of the test section, very close to the inlet to ensure freestream laminar conditions. A pitot-static tube was used to measure the incoming velocity at hub-height and hotwire measurements were taken $2d$ downwind of turbine to obtain the velocity profile. The voltage signal from turbine was sampled at 2 kHz. The rotational frequency of the turbine was measured using a Laser Tachometer. This process was repeated for various incoming velocities. The thrust coefficient (C_T) and the aerodynamic power coefficient ($C_{P_{aero}}$) of the turbine were calculated from the wake velocity profile using the following set of equations.

$$\begin{aligned} C_T &= 2T/\left(\rho U_\infty^2 A_r\right) \\ T &= \int_{A_w} \rho U_w \left(U_\infty - U_w\right) dA \end{aligned} \tag{3.1}$$

$$\begin{aligned} C_{P_{aero}} &= 2P_{aero}/\left(\rho U_\infty^3 A_r\right) \\ P_{aero} &= \int_{A_w} \frac{1}{2}\rho U_w \left(U_\infty^2 - U_w^2\right) dA \end{aligned} \tag{3.2}$$

where ρ is the density of air, $A_r = \pi d^2/4$ is the rotor area, A_w is the wake area with radius defined by the perpendicular distance from rotor axis to the radial location where $U_w =$

$0.99U_\infty$; U_∞ is the mean incoming free-stream velocity and U_w is the mean velocity at a spatial point in the wake. The expressions for T and P_{aero} in the above equations are derived from momentum and energy balance, respectively applied to the Betz's streamtube. The integrals in the above equations are evaluated by considering the radial velocity distribution in the wake and using it to calculate the volume of revolution about the turbine axis. Figure 3.1a,b provides the values of C_T and $C_{P_{aero}}$ with changing tip-speed ratio λ which resulted from the variation of the incoming velocity over the range $U_{hub} \in [4, 10]$ m s^{-1}.

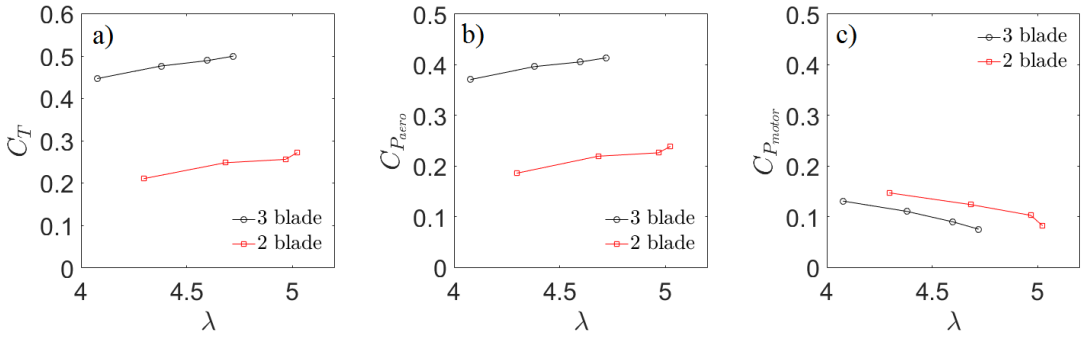

Figure 3.1: Single turbine performance characterization. a) Thrust coefficient C_T; b) aerodynamic power coefficient $C_{P_{aero}}$; c) actual power coefficient $C_{P_{motor}}$ as function of λ.

In addition to the power coefficient obtained from the wake velocity profile, C_P was also calculated based on the voltage output from the motor. The $C_{P_{motor}}$ was calculated using the first part of Equation 3.2, except P_{aero} is replaced in the formula with P_{motor}, which is obtained as described in Section 2.4. Figure 3.1c gives the actual turbine performance, which is evidently different from that obtained in Figure 3.1a. This is attributed to the intrinsic inefficiency of the generators at the given operating conditions [28].

The wake characteristics of the single 3- and 2-bladed turbines in turbulent boundary layer flow are described next. This is an important first step to analyze the differences in the flow characteristics of the individual turbines, before full-fledged experiments on their combined use in a farm setting can be justified. Figure 3.2 illustrates the normalized mean streamwise velocity distribution in the wake of a single 3-bladed and 2-bladed turbine.

Comparison of the two wakes show a marked difference in the mean velocity behind the two turbines up to a downwind distance of $4d - 5d$. This indicates the potential for improved power performance of the downwind turbine operating in the wake of a 2-bladed upwind turbine. The associated turbulence intensity is illustrated in Figure 3.3 for the two rotor types. The difference in turbulences levels are clearly observed up to intermediate downwind distances. The lower intensity induced by 2-bladed rotor might be eventually beneficial for downwind turbine in terms of reduced turbulent loading.

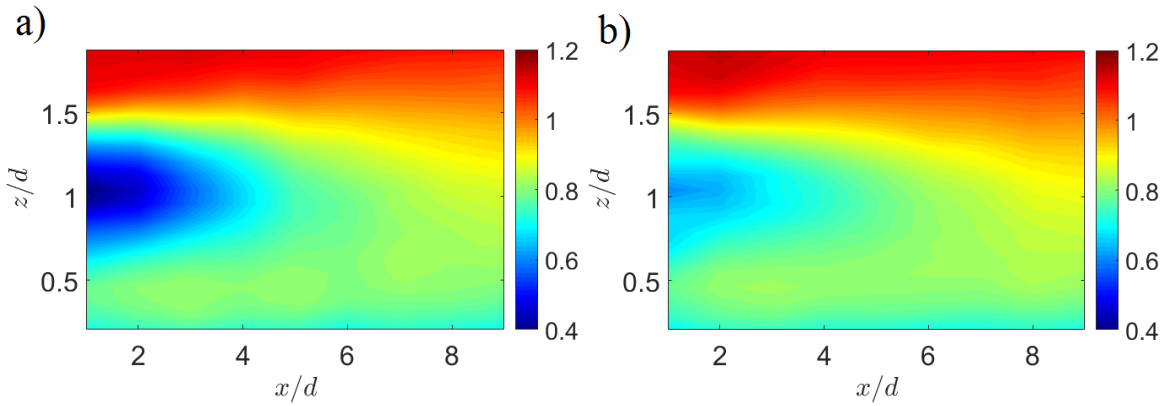

Figure 3.2: Normalized mean streamwise velocity distribution U/U_{hub} in the wake of a single 3-bladed (a) and 2-bladed (b) turbine along central vertical plane.

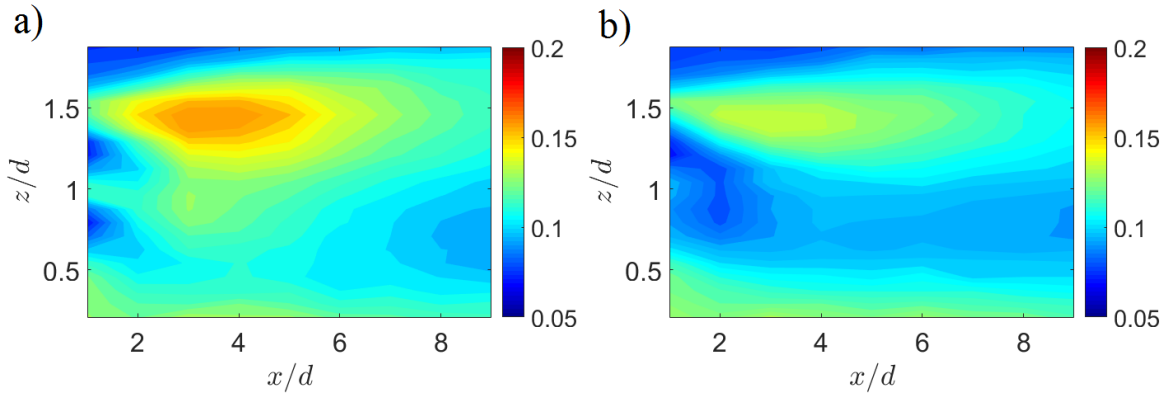

Figure 3.3: Turbulence intensity distribution σ_u/U_{hub} in the wake of a single 3-bladed (a) and 2-bladed (b) turbine along central vertical plane.

Chapter 4

Results And Discussion

In this section, we explore the potential benefits of the proposed hybrid farm (configuration-A) by performing a comparative analysis with the baseline case (configuration-B). The differences in the flow are described via the mean flow statistics, integral length scale and spectral decomposition of the flow; whereas the difference in performance characteristics is presented through turbine power analysis. For the sake of brevity, the results most relevant to the goal of this study are represented using either one of the two streamwise spacing (S_x) scenarios unless there is a difference worth pointing it out.

4.1 Mean flow and turbulence statistics

First, the mean streamwise velocity component within the configurations A and B are compared by calculating the $\Delta U/U_{hub}$ defined as:

$$\Delta U/U_{hub} = U_A/U_{hub} - U_B/U_{hub} \tag{4.1}$$

where U_A is the mean streamwise velocity at a given spatial location in configuration A and U_B is the counterpart velocity corresponding to the same point in configuration B. The spatial distribution of U/U_{hub} in the vertical plane at $y = 0$ is shown in Figure 4.1 for S_x = 5 and 10. It clearly shows that for S_x = 5, there is a significant difference in streamwise velocity in the rotor-swept wake of 2-bladed turbines in configuration-A as compared with the 3-bladed counterpart in configuration-B (corresponds to the even numbered rows). This is particularly prominent in the near wake, where velocity of configuration-A exceeds that

of configuration-B by up to 15% of U_{hub}. However, this difference quickly diminishes downwind, so that only differences of up to 5% of U_{hub} are observed $1d$ upwind of the rotor of the downwind turbines. It is worth noting that for $S_x = 5$, deeper into the wind farm, $\Delta U/U_{hub}$ is no longer negligible behind odd turbine rows (which correspond to 3-bladed turbines in both configurations). This suggests that the larger momentum in the wake of upwind 2-bladed turbines permeates through downwind turbines. For $S_x = 10$, the difference in the streamwise velocities behind even numbered rows is only restricted to the near wake and is minimum right upwind of the rotor of the downwind turbines. This is because the larger S_x in this case allows the wake flow to interact with the outer flow more efficiently, leading to equal recovery in both configurations. This suggests that, from the power output optimization standpoint, any potential benefits associated with 2-bladed rotors are reduced when streamwise spacing is around $10d$.

The turbulence intensity of the two configurations is compared next in Figure 4.2. Only $S_x = 5$ case is shown here because $S_x = 10$ case does not show distinctive insight, as expected. The difference in turbulence intensity is defined as follows:

$$\Delta I = sign(\sigma_B^2 - \sigma_A^2) \times \frac{\left(|\ \sigma_B^2 - \sigma_A^2\ |\right)^{1/2}}{U_{hub}} \tag{4.2}$$

where σ's here represent standard deviation of streamwise velocity component. From Figure 4.2, reduction in turbulence levels of up to 6% are observed in the flow impinging the turbines immediately downwind of 2-bladed units in configuration-A as compared with configuration-B. Furthermore, this effect persists beyond the adjacent rows into the wake of the downwind row, resulting in up to 4% reduction in I for the incoming flow to the next 2-bladed turbine row. The overall lower turbulence intensity of configuration-A is expected to result in a lower flow-induced turbulent loading on the turbines (not taking into account the difference in dynamic characteristics of the 2-bladed and 3-bladed rotors due to difference in inertia) and thus a longer fatigue life [29].

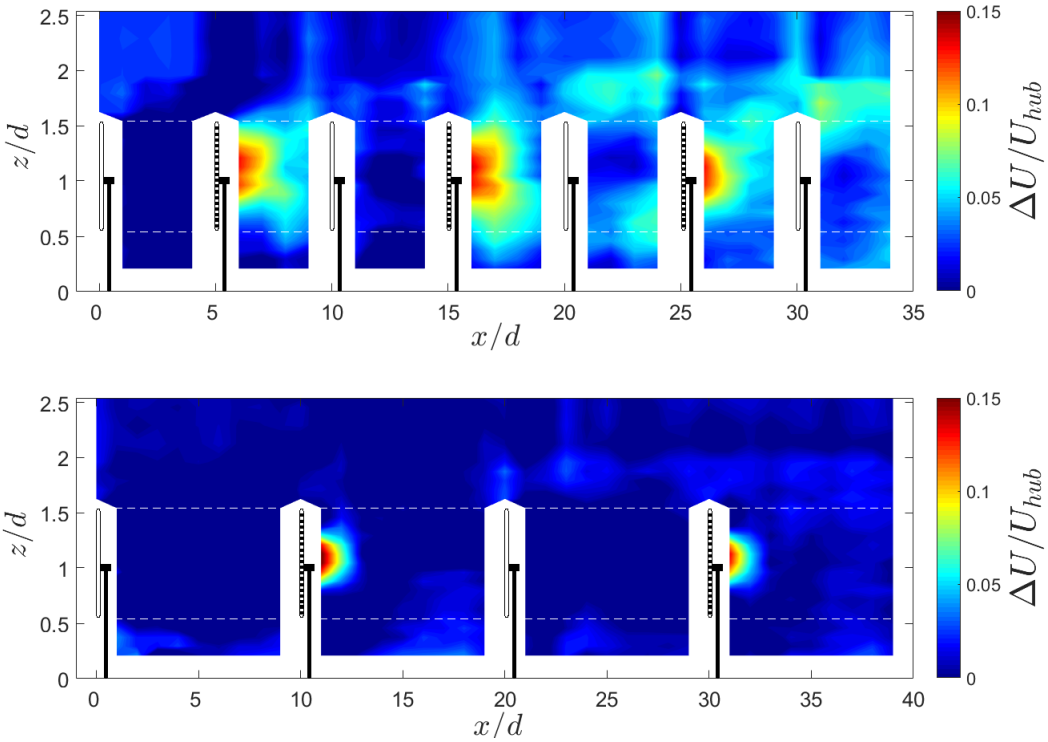

Figure 4.1: Distribution of the normalized mean streamwise velocity difference $\Delta U/U_{hub}$ between configuration-A and configuration-B in the vertical plane at $y = 0$ for $S_x = 5$ (top) and $S_x = 10$ (bottom). The horizontal dashed lines represent top and bottom tip heights. Striped rotors are used to represent comparison between non-identically bladed rotors across the two configurations.

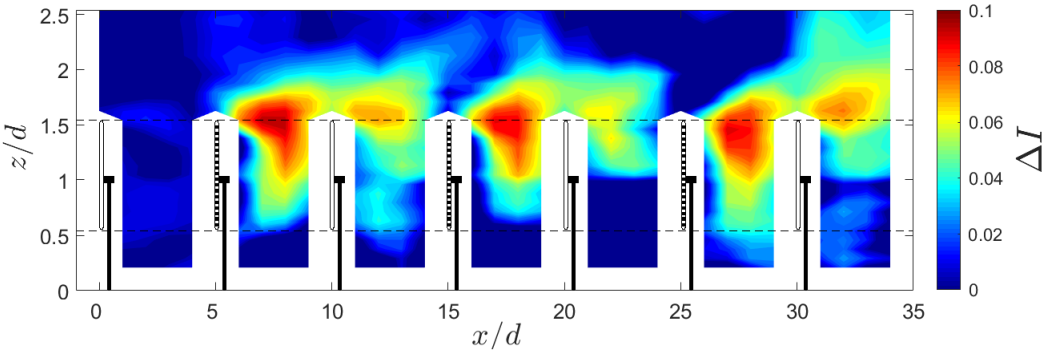

Figure 4.2: Distribution of the turbulence intensity difference ΔI between configuration-B and configuration-A in the vertical plane at $y = 0$ for $S_x = 5$.

4.2 Integral length scale

In this subsection and the subsequent one, we investigate the distinctive effects of the blade number on the structure of the wake flow and the relative importance of different scales of the turbulent flow. In this regard, the first quantity inspected is the integral length scale, which represents the characteristic large scale. It provides a bulk parameter to study the effect of turbulent scales on the flow. The integral length scale Λ^u is estimated from the local convection velocity and autocorrelation function of the streamwise velocity fluctuations $r(\tau)$, by using Taylor's frozen field hypothesis, as follows:

$$\begin{aligned} r(\tau) &= \overline{u'(t)\,u'(t-\tau)}/\sigma_u^2 \\ \mathscr{T}^u &= \int_0^\infty r(\tau)\,d\tau \\ \Lambda^u &= U_c \mathscr{T}^u \end{aligned} \tag{4.3}$$

where τ is the time lag of velocity signal, u' is the streamwise velocity fluctuation, σ_u^2 is the corresponding velocity variance, U_c is the convective velocity and $\mathscr{T}^u$ is the integral time scale. Here, the convective velocity U_c is approximated by the local streamwise velocity U. Following the approach adopted by Chamorro *et al.* [30], a threshold value of $r = 0.05$ is selected to evaluate the integral in equation 4.3. The profile of Λ^u of the incoming flow normalized by that at the hub height, $\Lambda^u_{hub}/d \approx 1.3$, is illustrated in figure 2.4c.

Spatial distribution of the integral length scale for the configuration-A normalized with incoming integral length scale Λ^u_{inc} at corresponding height, is shown in Figure 4.3 for $S_x = 5$. It shows a large reduction of the integral length scale in the near wake of turbine in the rotor-swept area and recovery of only up to 35% of Λ^u_{inc} are observed at the downwind turbine locations. Figure 4.3 also shows the difference of normalized integral length scale across the two configurations defined as:

$$\Delta\Lambda^u/\Lambda^u_{inc} = \Lambda^u_A/\Lambda^u_{inc} - \Lambda^u_B/\Lambda^u_{inc} \tag{4.4}$$

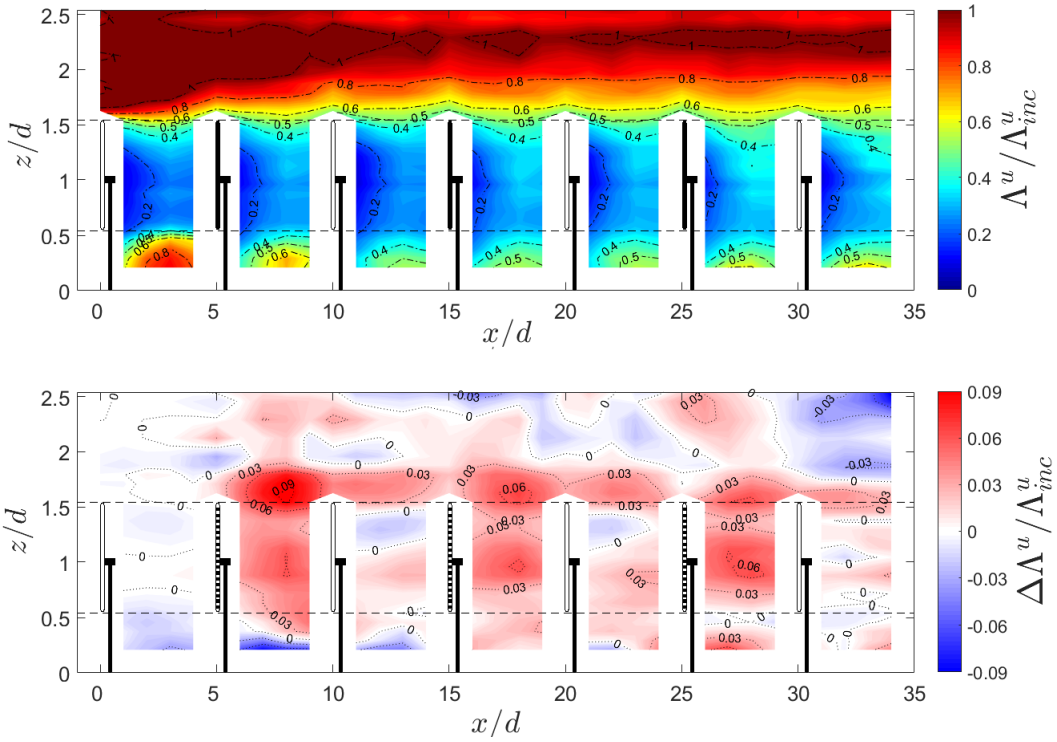

Figure 4.3: Isocontours of normalized Integral length scale for configuration-A (top) and the difference of normalized Integral length scale between configuration-A and configuration-B (bottom), in the vertical plane at $y = 0$ for $S_x = 5$. Filled rotors in top figure represent 2-bladed turbines, while the striped rotors in bottom figure are defined the same way as in Figure 4.1.

It is evident from Figure 4.3 that the representative large scale differ moderately behind 2-bladed and 3-bladed turbines. This difference is particularly prominent at hub-height and top-tip height, where vortices from tip and root of the blade are expected to be present, without being significantly dampened by the wall effect. This is indicative of the difference in vortex strength of the two types of rotors. It is also worth noting that the difference in integral length scale is the largest behind the second row and it diminishes for the down-wind rows. This can be explained by the fact that very large scale eddies contained in the incoming turbulent flow have impact only for the first few rows and downwind, these

eddies are systematically broken down into smaller eddies by the active modulation of the turbines [31, 32], resulting in smaller turbulent scales impinging the turbines deep inside the farm. As we will discuss in the subsequent section, 2-bladed turbines are less effective than 3-bladed ones in adding more energy to relatively smaller scales. Therefore, the large scale structures in the incoming flow still have a dominant contribution to integral length scale behind the first row of 2-bladed turbines, resulting in larger difference behind the second row; whereas for the forth and sixth rows, the flow is comparatively homogenized, so that fewer large scale structures remain in the flow to influence the integral length scale calculation behind these rows, thus the smaller difference between the two configurations.

4.3 Velocity Spectra

To gain a better insight into the relative importance of scales in determining contribution to integral length scales and overall turbulence level, we explored the distribution of spectral energy content across the scales in the wake flow. The normalized pre-multiplied spectral difference of streamwise velocity $\Delta(f\Phi_u)/u_*^2$, defined by Equation 4.5, between the two configurations A and B across frequencies and downwind distances is illustrated in Figure 4.4 for streamwise spacing scenario of $S_x = 5$.

$$\Delta(f\Phi_u)/u_*^2 = (f\Phi_B - f\Phi_A)/u_*^2 \tag{4.5}$$

Figure 4.4 reveals significant differences in the energy content of the scales which are known to modulate the structure of instantaneous power of the turbines [33]. At top tip height, the 2-bladed turbine wake clearly exhibits lower energy than 3-bladed counterpart, for the large-scale motions in the range $fd/U_{hub} \in [10^{-1}, 10^{0}]$. Furthermore, the effects of the lower energy are observed to penetrate through at least one adjacent downwind row. Within this range of frequencies, the difference is strikingly high for the scales on the order $\sim 0.2-0.3$ times of the rotor diameter. The large-scale motions within this subrange

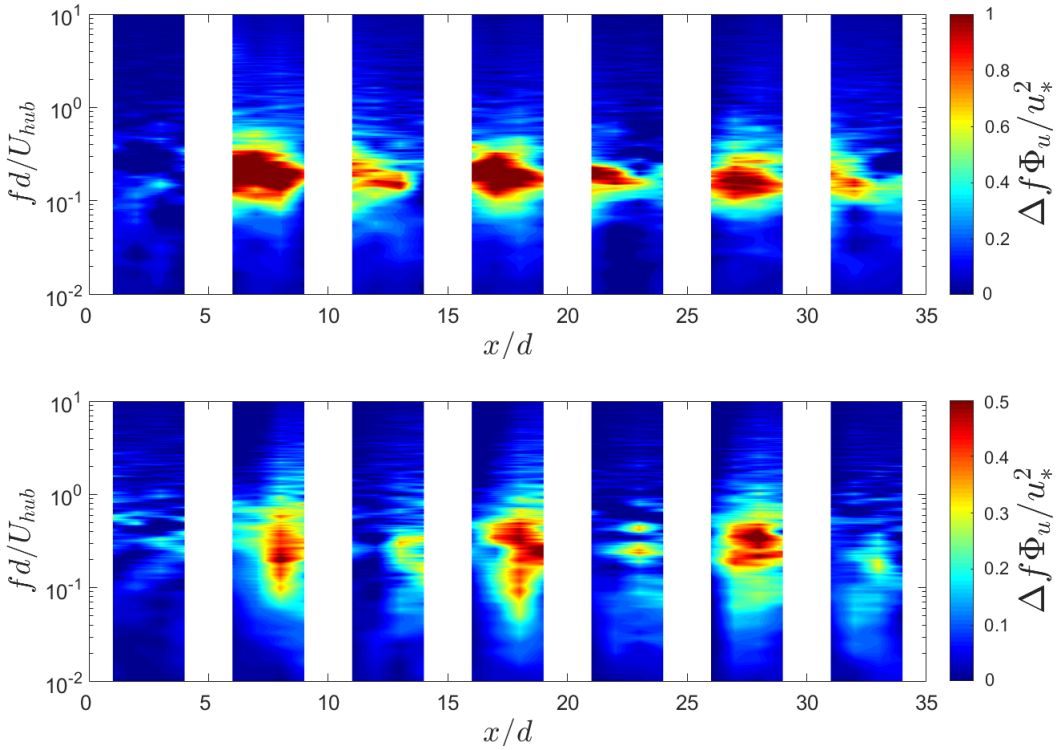

Figure 4.4: Contours of the pre-multiplied spectral difference of streamwise velocity component between configuration-A and configuration-B, $\Delta(f\Phi_u) = f\Phi_B - f\Phi_A$, normalized with square of friction velocity u_*, in $y = 0$ plane for $S_x = 5$ case at top tip height (top) and hub height (bottom).

have a special relevance for wind turbines, as elucidated in the subsequent paragraph. The difference in energy is again observed at hub height for a similar range of scales ($fd/U_{hub} \in [10^{-1}, 10^{0}]$), although at a lower magnitude (note the change in scale of the colorbar). However, here we do not see the subrange with very high difference as observed at top tip height and the effects of lower energy are attenuated beyond the adjacent downwind row. At the bottom tip height (not shown here), the pre-multiplied spectral difference between the two configurations is practically negligible, explained by the fact that in the vicinity of the wall, the structure of the flow is strongly modulated by the wall effects rather than geometry of the rotor.

To investigate the underlying phenomenon behind the spectral energy difference between the two configurations, the pre-multiplied velocity spectra at hub height in configuration-

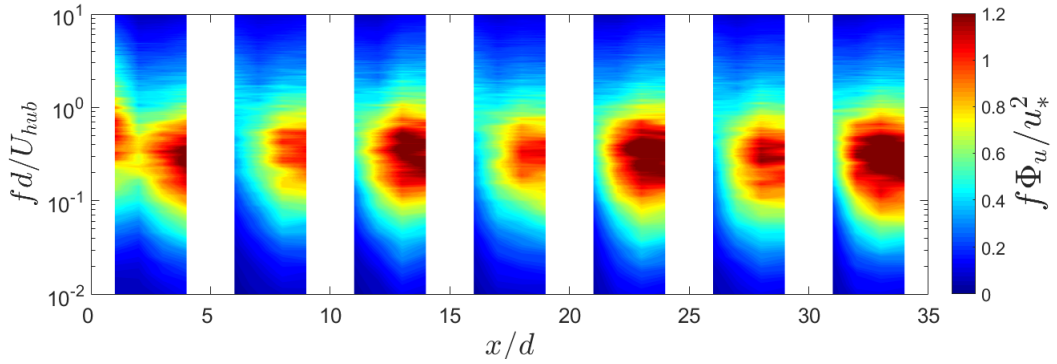

Figure 4.5: Normalized pre-multiplied velocity spectrum of configuration-A in $y = 0$ plane for $S_x = 5$ case at hub height.

A is presented in Figure 4.5. It can be observed that energy is being added to motions in the normalized frequency range of $fd/U_{hub} \in [10^{-1}, 10^{0}]$, as reported by Jin *et al.* [25] and also observed in experiments by Chamorro *et al.* [31]. A closer inspection of Figure 4.5 reveals that in this range, the spectral energy contribution of 2-bladed rotors is lower than 3-bladed ones, indicating the lower effectiveness of 2-bladed rotors in exciting the intermediary scales on the order of rotor diameter. This gives an indication that "active-filter" nature of turbine (as defined by Chamorro *et al.* [31]) is a function of blade number, and that 2-bladed rotors are less "active" than 3-bladed counterpart. Although this explains the general difference in spectral energy observed at hub and top-tip height in the range of $fd/U_{hub} \in [10^{-1}, 10^{0}]$ in Figure 4.4, the additional difference at top tip height in the subrange of $fd/U_{hub} \in [0.2, 0.3]$ is still unaccounted for. Figure 4.6a illustrates the streamwise evolution of pre-multiplied spectral contribution at top-tip height for the two configurations. It is evident from the figure that 3-bladed turbines exhibit a stronger interaction with the very large scales as compared with 2-bladed turbines. A selected pre-multiplied spectrum at $x/d = 16$ is illustrated in Figure 4.6b to show the peak and its corresponding distribution more clearly. The peak of pre-multiplied spectrum is observed to be at normalized frequency of $fd/U_{hub} \approx 0.2$, which corresponds to a Strouhal number of $St = fd/U_{hub,local} \approx 0.26$, where $U_{hub,local}$ is the incoming velocity at hub-height seen

by the local turbine. The occurrence of peak at $St \approx 0.26$ in this plot, where the background turbulent flow has been filtered out, indicates that these scales originate from the interaction of flow with turbines and are possibly associated with wake meandering. The value of Strouhal number for meandering observed here is consistent with those reported in the past wind tunnel studies on single turbines [34–36] and model wind farms [37]. Note that the meandering effect seems to be spread over a narrow range of low frequencies rather than appearing as a distinct narrow peak in the streamwise velocity spectrum. Similar observations were made by Coudou *et al*. [37] at top-tip height in their experiments. It is worth pointing that here the meandering refers to the large scale vortex shedding type instability similiar to that in bluff-body as reported in the past for model wind turbines by various authors [34, 38], rather than the one observed in full-scale wind turbines in field, where meandering is attributed to large scale fluctuations of incoming atmospheric boundary layer [39]. The absence of this effect at hub and bottom-tip heights can be attributed to the strong modulation of wall roughness at these heights which has been shown to suppress the meandering effect [35].

Referring back to Figure 4.6a, with increasing downwind row number, the meandering effect in configuration-B appears to be amplified while its intensity is regulated by the presence of 2-bladed turbines in configuration-A. Two possible explanations for reduced vortex shedding strength of 2-bladed turbine are proposed. First, the relatively lower vortex pitch (distance between consecutive helical vortices) of the 2-bladed turbines results in weaker interaction between the tip-vortices in the near wake, which are thought to give rise of large-scale vortex shedding; secondly, the lower solidity of 2-bladed rotor should result in lower strength of shed vortex, similar to that observed for high-porosity discs in [40]. However, the amplification of meandering starts diminishing after the fifth row, possibly due to homogenization of the wake and absence of any incoming large eddies at this depth, which are essential for meandering [41]. Thus, it can be concluded that placing 2-bladed turbines between rows of 3-bladed ones can breakdown the strong large-

scale interactions between adjacent rows of 3-bladed turbines, resulting in dampening of energetic motions, which might be responsible for large power fluctuations and fatigue loads. The overall spectral energy difference between the two configurations near the top-tip height is a superposition of two distinct contributions, one from the difference in typical active turbulence generator nature and the other from the difference in meandering effect of rotors differing in blade number.

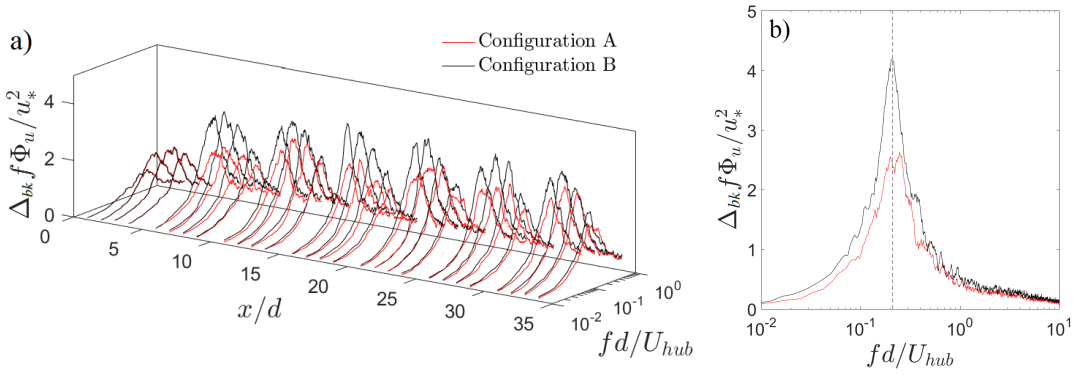

Figure 4.6: Normalized pre-multiplied spectral difference, $\Delta_{bk}(f\Phi_u)/u_*^2 = (f\Phi - f\Phi_{bk})/u_*^2$, for configuration-A and configuration-B along the streamwise direction (a) and at $x/d = 16$ (b). The vertical dashed line in b) shows the meandering frequency $f_m d/U_{hub} \approx 0.2$. Scenario: Top tip height, $y = 0$ plane, $S_x = 5$.

As discussed in section 4.1, the $S_x = 10$ case has no evident benefits on the flow characteristics of the wake in a mean sense, in relation to the performance of turbines. However, it is worth looking at the structural content of the flow in this case, to explore any potential positive effects from the flow structure point of view. Figure 4.7 provides a comparison of the background flow removed pre-multiplied spectral distribution, between $S_x = 5$ and $S_x = 10$ cases for configuration A at bottom-tip height. In both cases, energy is being removed from very large scales at all downwind distances, as reported by Chamorro *et al.* [31]; while energy is added to very small scales in the very near wake ($x/d = 1$) of the turbine. Additionally, for $S_x = 5$ case, energy is also added to intermediate scales throughout the downwind distances, as also discussed previously for hub-height. This indicates that for smaller streamwise spacing, these intermediate scales persist up to adjacent downwind

rows. This effect keeps accumulating deeper into the farm because the downwind turbines are subject to stronger medium to large scale motions, resulting in even stronger interaction of these scales with the downwind turbines. This is consistent with Jin *et al.* [25], who reported a stronger interaction between large scales and turbine under high incoming turbulence. For the $S_x = 10$ case, this effect is absent because the increased turbulent kinetic energy of wake flow due to flow-turbine interaction dies off at longer distances downwind [25]. Thus, $S_x = 10$ scenario does not present very distinctive dynamics with regard to the use of non-identical rotors in the array, since the streamwise adjacent turbine rows seem to be isolated from each other, both in a mean and structural sense.

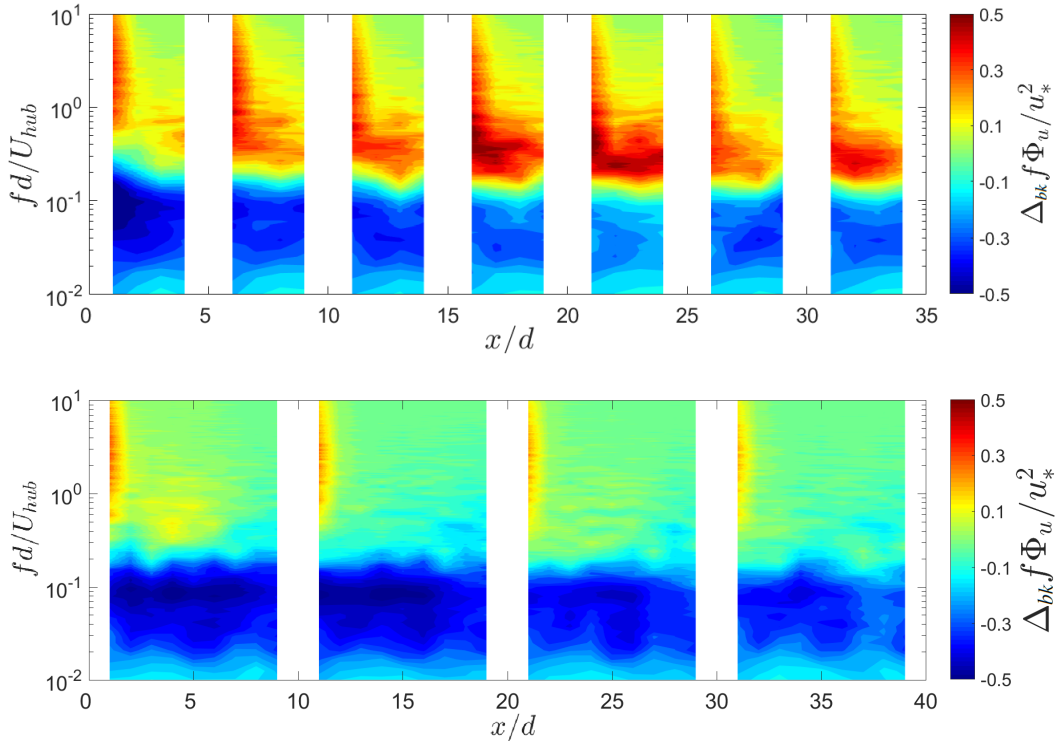

Figure 4.7: Normalized pre-multiplied spectral difference of configuration-A with background flow, $\Delta_{bk}(f\Phi_u)/u_*^2 = (f\Phi_A - f\Phi_{bk})/u_*^2$, for $S_x = 5$ (top) and $S_x = 10$ (bottom), at bottom tip height in $y = 0$ plane.

Finally, it is worth discussing here the mean wake flow recovery behavior in the light of flow-structure. Figure 4.8 illustrates the streamwise distribution of mean streamwise velocity component at hub-height, top-tip height and a height above the wind farm for $S_x = 5$

case. At hub-height, the 3-bladed rotor clearly has a higher recovery rate of mean velocity than 2-bladed one, although the streamwise distance of 5 rotor diameters is still insufficient for the wake velocity of 3-bladed rotor to recover to the same level as 2-bladed one. The better recovery rate of configuration-B can be attributed to the fact that in this case, the higher turbulent energy in large scales, especially at top-tip height (as seen previously in Figure 4.4), causes better mixing between the outer energetic flow and the wake. The improved mixing effect can also be inferred by comparing the velocity distribution above the farm in Figure 4.8. It is clear that at this height, configuration-B has a greater decay of velocity than configuration-A, indicating a larger wake expansion in configuration-B, which follows directly from better mixing between outer and inner flows. Similar observations were made regarding the difference in recovery rate and wake expansion of two and three bladed turbines by Medici *et al*. [19].

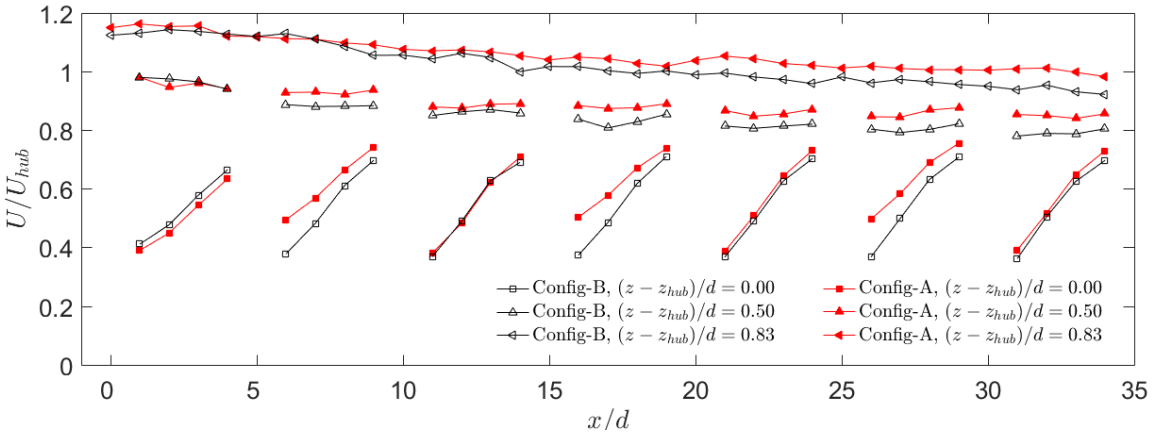

Figure 4.8: Normalized streamwise velocity distribution for $S_x = 5$ in central plane.

4.4 Turbine power analysis

In this subsection we evaluate the power performance of turbines by analyzing the mean statistics and spectrum of the voltage signal from the generators of the central turbines in each row. Figure 4.9 illustrates the distribution of normalized mean power and power

fluctuation intensity in the farm. The mean power has been normalized with $\overline{P}_{single}$, the mean power of a corresponding two or three-bladed single turbine operating in the background turbulent boundary layer flow, where $\overline{P}_{single} \approx 0.43$ W and 0.58 W for three and two bladed turbine, respectively. In $S_x = 5$ case, for both types of rotor the mean power reaches a respective equilibrium value from 2^{nd} row onwards, in both configurations. In Configuration-A, the 3-bladed turbines immediately behind the 2-bladed ones appear to perform slightly better than their counterparts in configuration B, due to higher momentum available in the wake of 2-bladed rotors, as seen in Figure 4.8. However, the resulting marginal gain in the mean power output of the farm in configuration A is possibly offset by the slight under-performance of 2-bladed turbines as compared with 3-bladed ones inside the farm. In the $S_x = 10$ case, consistent with the observations made in section 4.1, there is negligible difference between the two configurations with respect to mean power performance for the first three rows; the mean power of 2-bladed turbine is actually reduced deep inside the farm.

In general, the intensity of power fluctuation decreases after the first row, as the large-scale structures in the incoming flow are dampened by the first row (see Figure 4.7). From that point onward, I_p gradually increases for $S_x = 5$, possibly due to better mixing of wake with the outer flow at downwind locations in the farm, and attains an equilibrium value around 6^{th} row, whereas for $S_x = 10$, equilibrium appears to be attained from 2^{nd} row onward. The fluctuations of 2-bladed turbines are in general greater than 3-bladed turbines; in particular for $S_x = 10$, this difference is significantly higher, possibly due to pronounced effect of load imbalance for 2-bladed rotor at higher velocities faced by the turbines in this case and due to lower inertia of the 2-bladed rotor, which makes it more susceptible to turbulent loading. However, the 3-bladed turbines downwind of 2-bladed ones in configuration-A show somewhat lower fluctuation intensity than their counterparts in configuration-B, consistent with diminished turbulence intensity in the wake of 2-bladed turbine. The difference in intensity appears to die out deep inside the farm (row 6 & 7)

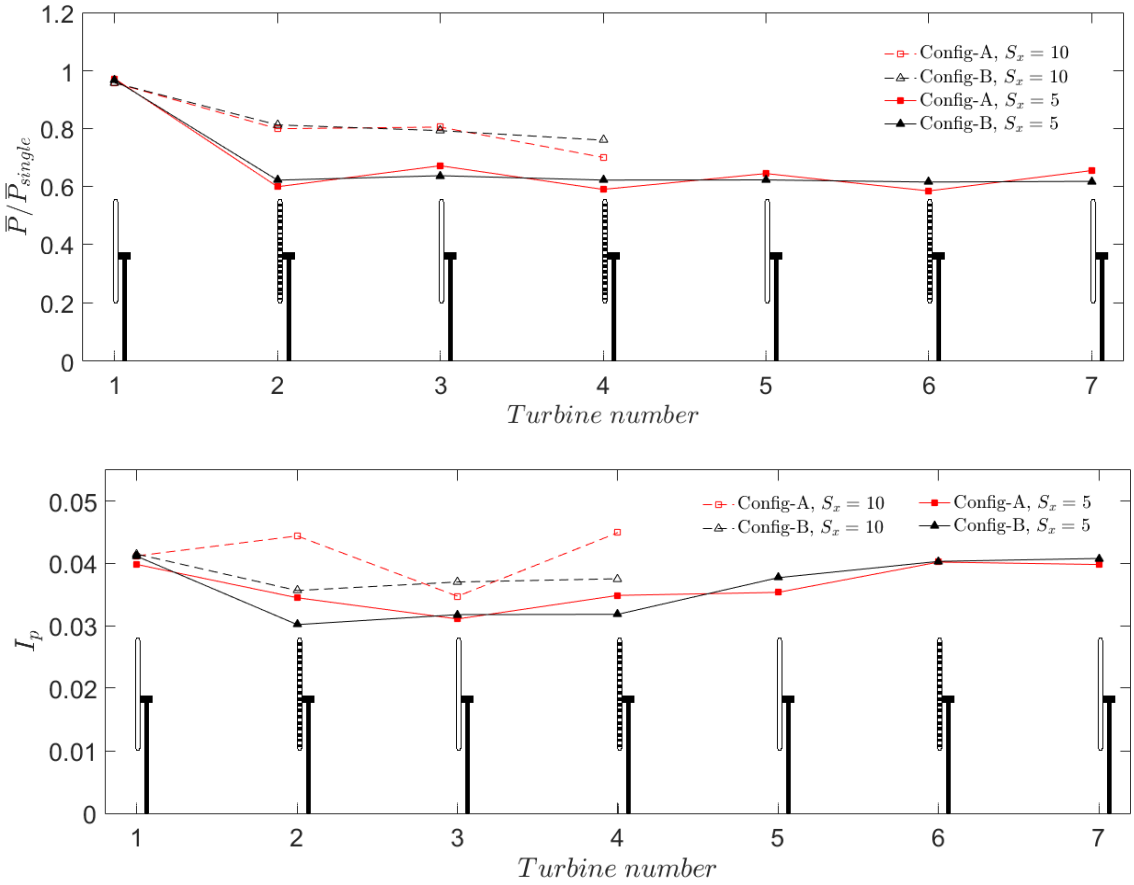

Figure 4.9: Power statistics for all tested configurations: Mean power of turbines normalized by that of a single turbine with the same number of blades operating in the background boundary layer turbulent flow $\overline{P}/\overline{P}_{single}$ (top) and the corresponding distribution of power fluctuation intensity, $I_p = \sigma_p/\overline{P}$ (bottom). Striped rotors have the same meaning as defined in Figure 4.1.

possibly due to homogenization of wake. The overall fluctuation intensity of the wind farm for all cases is presented in Table 4.1 using Equation 4.6. This equation takes into account the covariance of turbine pairs based on the fact that turbines in close proximity respond to the large-scale motions simultaneously [28]. The competing effects of the two rotors namely the higher I_p of 2-bladed rotor and the lower I_p of 3-bladed rotor operating in 2-bladed turbine's wake, result in overall power fluctuations of the wind farm $I_{p,farm}$ for configuration-A being comparable to that of configuration-B. The slightly higher $I_{p,farm}$ for configuration-A in $S_x = 5$ case may be attributed to the stronger coupling between

consecutive turbine fluctuations due to larger integral length scale for this configuration, as observed in Figure 4.3. The higher values of $I_{p,farm}$ for $S_x = 10$ as compared with $S_x = 5$ are consistent with the better entrainment of large energetic motions from outer flow into the wake, over longer recovery distances in $S_x = 10$ case. It can thus be concluded that although 2-bladed turbines evidently have a more advantageous flow structure than 3-bladed turbines from a turbulent loading standpoint, the fluctuations in power of the turbines seem to be dominated by structural properties of rotor rather than the impact of flow structure.

$$
\begin{aligned}
I_{p,farm} &= \left(\sigma^2\left(\sum_{i=1}^{N} P_i\right)\right)^{1/2} \Big/ \sum_{i=1}^{N} \overline{P}_i \\
\sigma^2\left(\sum_{i=1}^{N} P_i\right) &= \sum_{i=1}^{N} \sigma_{P_i}^2 + 2\sum_{i=1}^{N}\sum_{j>i}^{N} Cov\left(P_i, P_j\right)
\end{aligned}
\tag{4.6}
$$

Table 4.1: Total power fluctuation of wind farm

Configuration	S_x	$I_{p,farm}$
A	5	0.032
B	5	0.029
A	10	0.034
B	10	0.034

To investigate the structure of instantaneous turbine power and the effect of incoming flow structure on it, we show the spectral energy density of power output signal (Φ_p) from the generator and that of approach velocity (Φ_u) at hub-height in Figure 4.10, for configuration A $S_x = 5$ case. In Figure 4.10a we can clearly see the difference in structure of the approach flow between first and second row. The approach velocity to the first row exhibits higher spectral energy content in very large scale structures as compared with second row while for the second row, more energy is added to the intermediate and smaller scales. Note that for the second row, the inertial subrange of flow starts at a higher frequency as compared with the first row. The changes in flow structure are seen to have a direct influ-

ence on the structure of power fluctuations, consistent with previous studies by Chamorro *et al*. [13, 33], where the modulation of turbine power by the incoming hub-height velocity has been well established. They reported a damping/transfer function $G(f) \propto f^{-2}$ for the intermediate frequencies, which accounts for non-linear response of the turbine power to the flow defined as $\Phi_p = G(f)\Phi_u$. The spectra of power in Figure 4.10 follow this trend, with a power law decay of f^{-2} and $f^{-5/3-2}$ in frequency range below and within inertial subrange, respectively. Consistent with the structure of incoming flow, the region of power spectrum with $f^{-5/3-2}$ power law decay is shifted to higher frequencies for second turbine as compared with first turbine. Furthermore, the spectral content of power of second turbine shows less energetic large scales than that of first turbine, due to the dampening of large scale motions in the incoming flow to the farm by the first row. Comparison of spectra between fifth and sixth row in Figure 4.10b shows an increase in spectral energy content of power across all scales for 2-bladed turbine, even though the approach velocity to both rows has similar levels of energy density, especially at intermediate and small scales. This reiterates the point made earlier regarding the dominance of structural properties of rotor over flow structure in determining the behavior of power fluctuations.

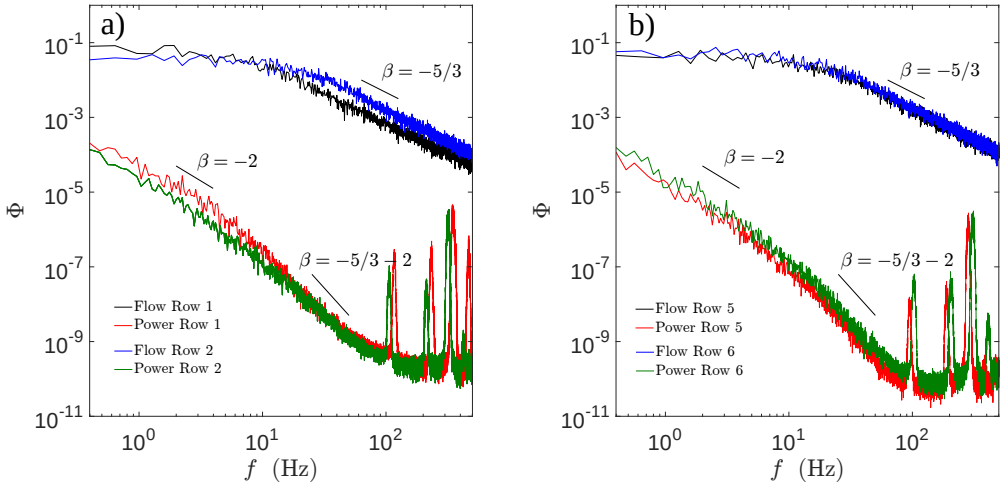

Figure 4.10: Power spectra of instantaneous turbine power and that of approach hub-height velocity $1d$ upwind of turbines, for a) first and second rows; b) fifth and sixth rows.

Chapter 5

Conclusions

The power and wake characteristics of a hybrid model wind farm with alternating rows of 3-bladed and 2-bladed turbines were investigated and compared with those of a baseline model farm composed of all 3-bladed turbines, for two values of streamwise turbine spacing S_x. For $S_x = 5$, the hybrid farm exhibited enhanced mean velocity in the wake and possibly lower flow-induced turbulent loadings on downwind turbines due to lower turbulence levels. The integral length scale and spectral analysis shed light on the difference in active effect of the two types of rotors, which leads to major structural differences in the wake flow. Additionally, the lower strength of bluff-body meandering at top-tip height for 2-bladed rotor prevents the large scales from amplifying as in configuration-B, thus resulting in reduced mixing for configuration-A and a lower recovery rate. Despite the presence of 2-bladed turbines in configuration-A showing beneficial effect on flow structure with regard to turbulent loading of turbines, the effect was not clearly translated in power fluctuation intensity, indicating a dominant role of the structural characteristics of rotor in determining the power fluctuations. A marginal increase in power output of 3-bladed turbines operating in the higher momentum wake of 2-bladed ones, is offset by the diminished performance of 2-bladed turbines inside the farm. For $S_x = 10$, the potential benefits associated with hybrid farm design are eliminated due to longer recovery distances resulting in uncoupled behavior of consecutive turbine rows.

Although the power performance of the proposed hybrid wind farm does not seem to improve over the baseline case, it can be argued that even a comparable performance of the hybrid design as observed in this study can prove to be cost-effective. One immediate

economic advantage is the lower manufacturing and transportation cost of 2-bladed rotors due to one less blade, especially for offshore wind farms. A previous feasibility study reported that for off-shore wind farms, a 2-bladed turbine operating at higher tip-speed ratio than 3-bladed one has lower energy cost [16]. All the 2-bladed turbines in the current study were operating at a higher tip-speed ratio than 3-bladed turbines, possibly making the hybrid configuration more cost-effective than baseline, without any significant reduction in power performance. Furthermore, implementing load-reduction techniques like teetering hub in order to mitigate the effect of load imbalance on the 2-bladed rotor is expected to further improve the power performance of a proposed configuration over baseline case by reducing the higher inherent fluctuations of 2-bladed rotor. Alternatively, by operating the 2-bladed turbines at the same tip-speed ratio as 3-bladed ones, it is predicted that the flow behind 2-bladed rotor would achieve even higher momentum and lower intensity levels, possibly leading to overall improved power performance of hybrid design.

References

[1] R. Wiser, E. Lantz, T. Mai, J. Zayas, E. DeMeo, E. Eugeni, J. Lin-Powers, and R. Tusing, "Wind vision: A new era for wind power in the united states," *The Electricity Journal*, vol. 28, no. 9, pp. 120–132, 2015.

[2] W. Energy, "A vision for europe in 2030," *Advisory Council of the European Wind Energy Technology Platform*, 2006.

[3] Z. Wang, J. Shi, and Y. Zhao, "Technology roadmap: China wind energy development roadmap 2050," *International Energy Agency and Energy Research Institute, Paris, France*, p. 56, 2011.

[4] M. Z. Jacobson, M. A. Delucchi, Z. A. Bauer, S. C. Goodman, W. E. Chapman, M. A. Cameron, C. Bozonnat, L. Chobadi, H. A. Clonts, P. Enevoldsen, *et al.*, "100% clean and renewable wind, water, and sunlight all-sector energy roadmaps for 139 countries of the world," *Joule*, vol. 1, no. 1, pp. 108–121, 2017.

[5] S. Grady, M. Hussaini, and M. M. Abdullah, "Placement of wind turbines using genetic algorithms," *Renewable Energy*, vol. 30, no. 2, pp. 259–270, 2005.

[6] J. S. González, A. G. G. Rodriguez, J. C. Mora, J. R. Santos, and M. B. Payan, "Optimization of wind farm turbines layout using an evolutive algorithm," *Renewable Energy*, vol. 35, no. 8, pp. 1671–1681, 2010.

[7] G. Mosetti, C. Poloni, and B. Diviacco, "Optimization of wind turbine positioning in large windfarms by means of a genetic algorithm," *J Wind Eng Ind Aerod*, vol. 51, no. 1, pp. 105–116, 1994.

[8] S. Chowdhury, J. Zhang, A. Messac, and L. Castillo, "Unrestricted wind farm layout optimization (uwflo): Investigating key factors influencing the maximum power generation," *Renewable Energy*, vol. 38, no. 1, pp. 16–30, 2012.

[9] X. Yang, S. Kang, and F. Sotiropoulos, "Computational study and modeling of turbine spacing effects in infinite aligned wind farms," *Phys Fluids*, vol. 24, no. 11, p. 115107, 2012.

[10] M. Calaf, C. Meneveau, and J. Meyers, "Large eddy simulation study of fully developed wind-turbine array boundary layers," *Phys Fluids*, vol. 22, no. 1, p. 015110, 2010.

[11] J. Meyers and C. Meneveau, "Optimal turbine spacing in fully developed wind farm boundary layers," *Wind Energy*, vol. 15, no. 2, pp. 305–317, 2012.

[12] L. P. Chamorro, R. Arndt, and F. Sotiropoulos, "Turbulent flow properties around a staggered wind farm," *Bound-Lay Meteorol*, vol. 141, no. 3, pp. 349–367, 2011.

[13] L. P. Chamorro, N. Tobin, R. Arndt, and F. Sotiropoulos, "Variable-sized wind turbines are a possibility for wind farm optimization," *Wind Energy*, vol. 17, no. 10, pp. 1483–1494, 2014.

[14] M. Adaramola and P.-Å. Krogstad, "Experimental investigation of wake effects on wind turbine performance," *Renewable Energy*, vol. 36, no. 8, pp. 2078–2086, 2011.

[15] G. Corten, P. Schaak, and E. Bot, "More power and less loads in wind farms:heat and flux," in *European wind energy conference & exhibition, London, UK*, 2004.

[16] A. J. Paul, *A Comparative Analysis of the Two-Bladed and the Three-Bladed Wind Turbine for Offshore Wind Farms*. PhD thesis, Masters thesis, Technical University of Delft, 2010.

[17] Shikha, T. Bhatti, and D. Kothari, "New horizons for offshore wind energy: Shifting paradigms and challenges," *Energ Source*, vol. 27, no. 4, pp. 349–360, 2005.

[18] F. Mühle, M. S. Adaramola, and L. Sretran, "The effect of the number of blades on wind turbine wake-a comparison between 2-and 3-bladed rotors," in *J Phys Conf Ser*, vol. 753, p. 032017, IOP Publishing, 2016.

[19] D. Medici, *Experimental studies of wind turbine wakes: power optimisation and meandering*. PhD thesis, KTH, 2005.

[20] A. J. Newman, R. B. Cal, and L. Castillo, "Blade number effects in a scaled down wind farm," *Renewable Energy*, vol. 81, pp. 472–481, 2015.

[21] R. Adrian, C. Meinhart, and C. Tomkins, "Vortex organization in the outer region of the turbulent boundary layer," *J Fluid Mech*, vol. 422, pp. 1–54, 2000.

[22] E. Johnson, A. A. Fontaine, M. L. Jonson, R. S. Meyer, W. A. Straka, S. Young, C. van Dam, H. Shiu, and M. Barone, "A1: 8.7 scale water tunnel test of an axial flow water turbine," in *Proceedings of the 1rst Marine Energy Technology Symposium, METS13, Washington Dc*, 2013.

[23] H. Shiu, C. van Dam, E. Johnson, M. Barone, R. Phillips, W. Straka, A. Fontaine, and M. Jonson, "A design of a hydrofoil family for current-driven marine-hydrokinetic turbines," *In Proceedings of the 20th International Conference on Nuclear Engineering and the American Society of Mechanical Engineers 2012 Power Conference, Anaheim, CA, USA, 30 July–3 August*, pp. 839–847, 2012.

[24] N. Tobin, A. M. Hamed, and L. P. Chamorro, "An experimental study on the effects of winglets on the wake and performance of a model wind turbine," *Energies*, vol. 8, pp. 11955–11972, 2015.

[25] Y. Jin, H. Liu, R. Aggarwal, A. Singh, and L. P. Chamorro, "Effects of freestream turbulence in a model wind turbine wake," *Energies*, vol. 9, no. 10, p. 830, 2016.

[26] L. P. Chamorro and F. Porté-Agel, "A wind-tunnel investigation of wind-turbine wakes: Boundary-layer turbulence effects," *Bound-Lay Meteorol*, vol. 132, pp. 129–149, 2009.

[27] Y. Ohya, "Wind-tunnel study of atmospheric stable boundary layers over a rough surface," *Bound-Lay Meteorol*, vol. 98, no. 1, pp. 57–82, 2001.

[28] H. Liu, Y. Jin, N. Tobin, and L. P. Chamorro, "Towards uncovering the structure of power fluctuations of wind farms.." Accepted in Phys Rev E, 2017.

[29] A. Rosen and Y. Sheinman, "The power fluctuations of a wind turbine," *J Wind Eng Ind Aerod*, vol. 59, no. 1, pp. 51–68, 1996.

[30] L. Chamorro, C. Hill, S. Morton, C. Ellis, R. Arndt, and F. Sotiropoulos, "On the interaction between a turbulent open channel flow and an axial-flow turbine," *J Fluid Mech*, vol. 716, pp. 658–670, 2013.

[31] L. Chamorro, M. Guala, R. Arndt, and F. Sotiropoulos, "On the evolution of turbulent scales in the wake of a wind turbine model," *J Turbul*, no. 13, p. N27, 2012.

[32] A. Singh, K. B. Howard, and M. Guala, "On the homogenization of turbulent flow structures in the wake of a model wind turbine," *Phys Fluids*, vol. 26(2), p. 025103, 2014.

[33] L. P. Chamorro, S. J. Lee, D. Olsen, C. Milliren, J. Marr, R. E. A. Arndt, and F. Sotiropoulos, "Turbulence effects on a full–scale 2.5 mw horizontal–axis wind turbine under neutrally stratified conditions," *Wind Energy*, vol. 18(2), pp. 339–349, 2015.

[34] D. Medici and P. H. Alfredsson, "Measurements behind model wind turbines: further evidence of wake meandering," *Wind Energy*, vol. 11, no. 2, pp. 211–217, 2008.

[35] E. Barlas, S. Buckingham, and J. van Beeck, "Roughness effects on wind-turbine wake dynamics in a boundary-layer wind tunnel," *Bound-Lay Meteorol*, vol. 158, no. 1, pp. 27–42, 2016.

[36] V. L. Okulov, I. V. Naumov, R. F. Mikkelsen, I. K. Kabardin, and J. N. Sørensen, "A regular strouhal number for large-scale instability in the far wake of a rotor," *J Fluid Mech*, vol. 747, pp. 369–380, 2014.

[37] N. Coudou, S. Buckingham, and J. van Beeck, "Experimental study on the wind-turbine wake meandering inside a scale model wind farm placed in an atmospheric-boundary-layer wind tunnel," in *J Phys Conf Ser*, vol. 854, p. 012008, IOP Publishing, 2017.

[38] W. Zhang, C. D. Markfort, and F. Porté-Agel, "Near-wake flow structure downwind of a wind turbine in a turbulent boundary layer," *Exp Fluids*, vol. 52, no. 5, pp. 1219–1235, 2012.

[39] G. C. Larsen, H. A. Madsen, K. Thomsen, and T. J. Larsen, "Wake meandering: a pragmatic approach," *Wind energy*, vol. 11, no. 4, pp. 377–395, 2008.

[40] D. Medici and P. H. Alfredsson, "Wind turbine near wakes and comparisons to the wake behind a disc," in *43rd AIAA Aerospace Sciences Meeting and Exhibit-Meeting Papers*, pp. 15593–15604, 2005.

[41] G. España, S. Aubrun, S. Loyer, and P. Devinant, "Wind tunnel study of the wake meandering downstream of a modelled wind turbine as an effect of large scale turbulent eddies," *J Wind Eng Ind Aerod*, vol. 101, pp. 24–33, 2012.

Appendix A

Results in wall-parallel plane at hub-height

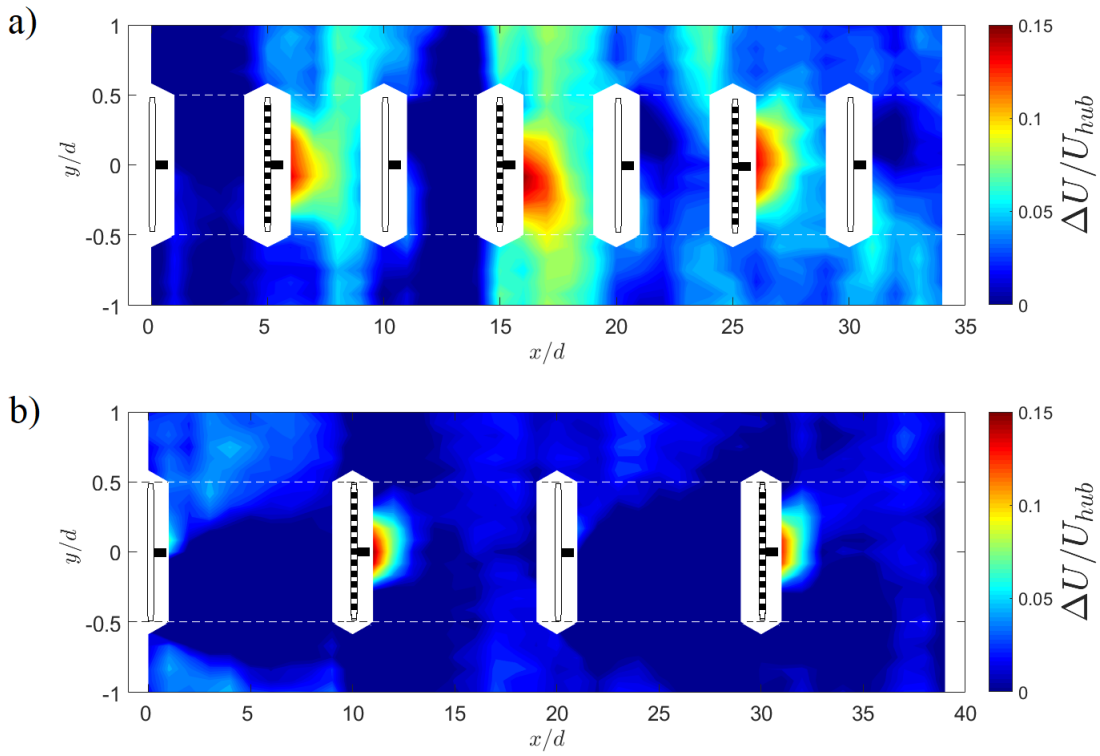

Figure A.1: Contours of mean streamwise velocity difference between two configurations ($U_A - U_B$) in wall parallel plane at hub-height for a) $S_x = 5$; b) $S_x = 10$.

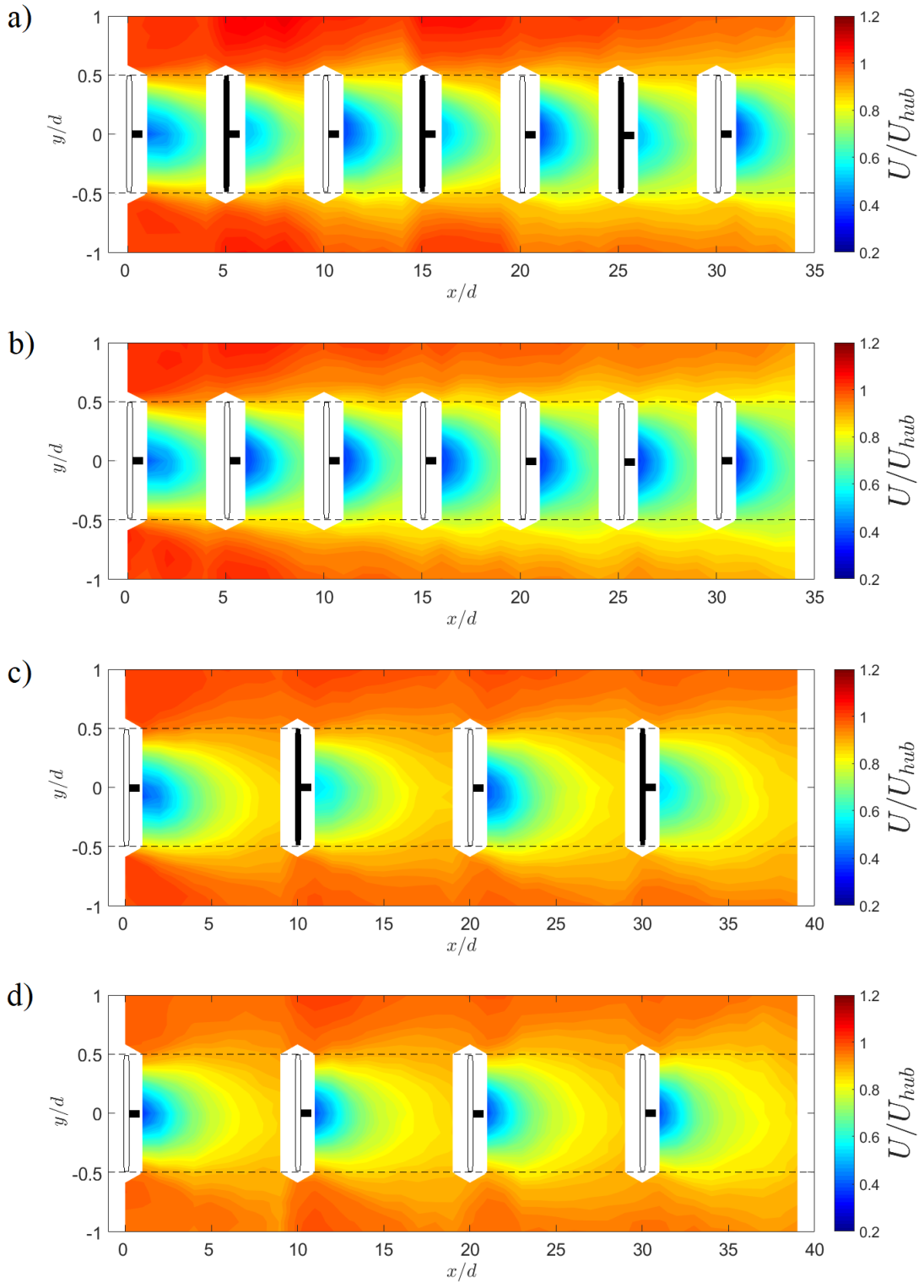

Figure A.2: Mean streamwise velocity contours in wall parallel plane at hub-height for a) configuration-A $S_x = 5$; b) configuration-B $S_x = 5$; c) configuration-A $S_x = 10$; d) configuration-B $S_x = 10$.

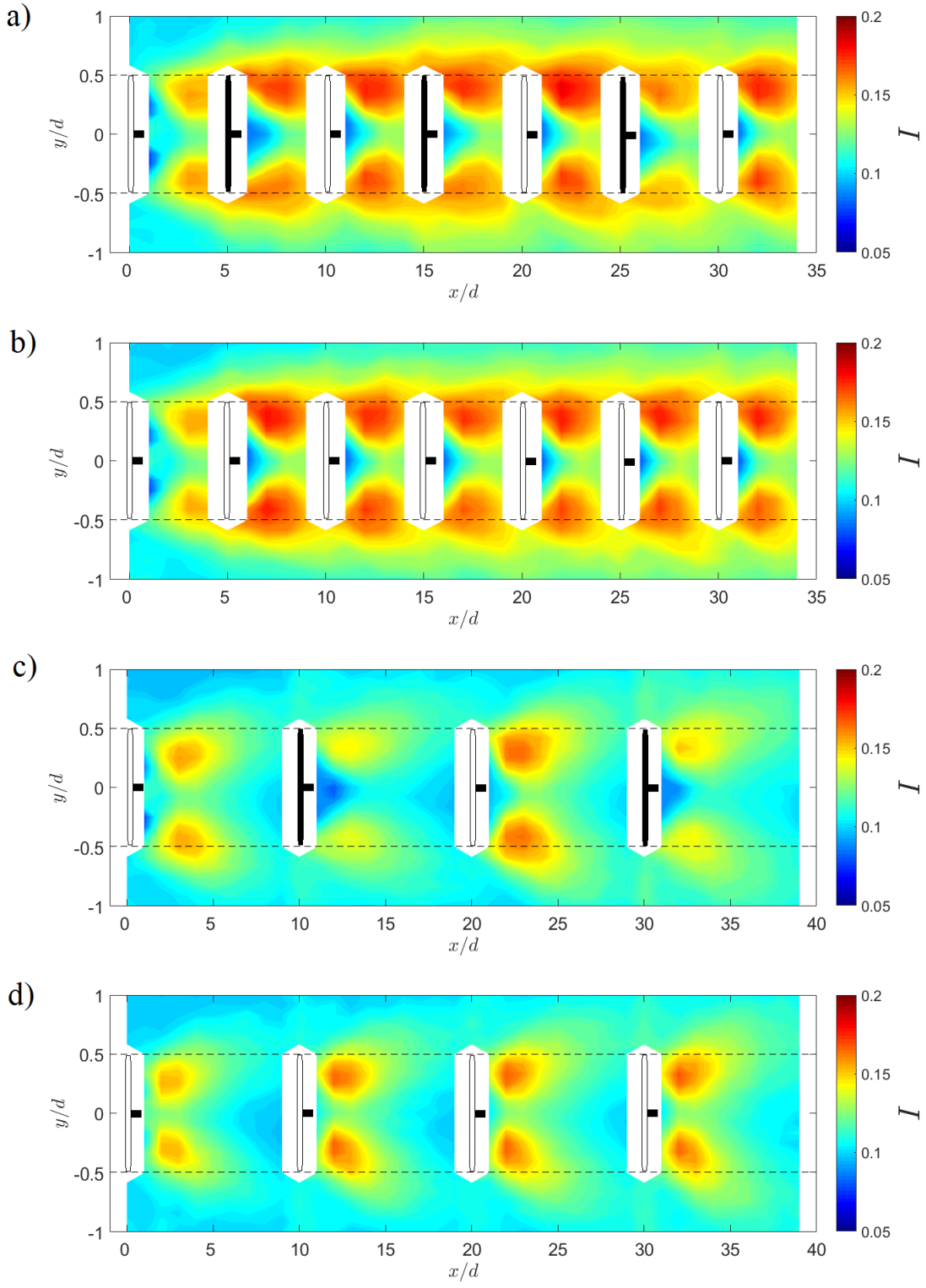

Figure A.3: Turbulence intensity contours in wall parallel plane at hub-height for a) configuration-A $S_x = 5$; b) configuration-B $S_x = 5$; c) configuration-A $S_x = 10$; d) configuration-B $S_x = 10$.

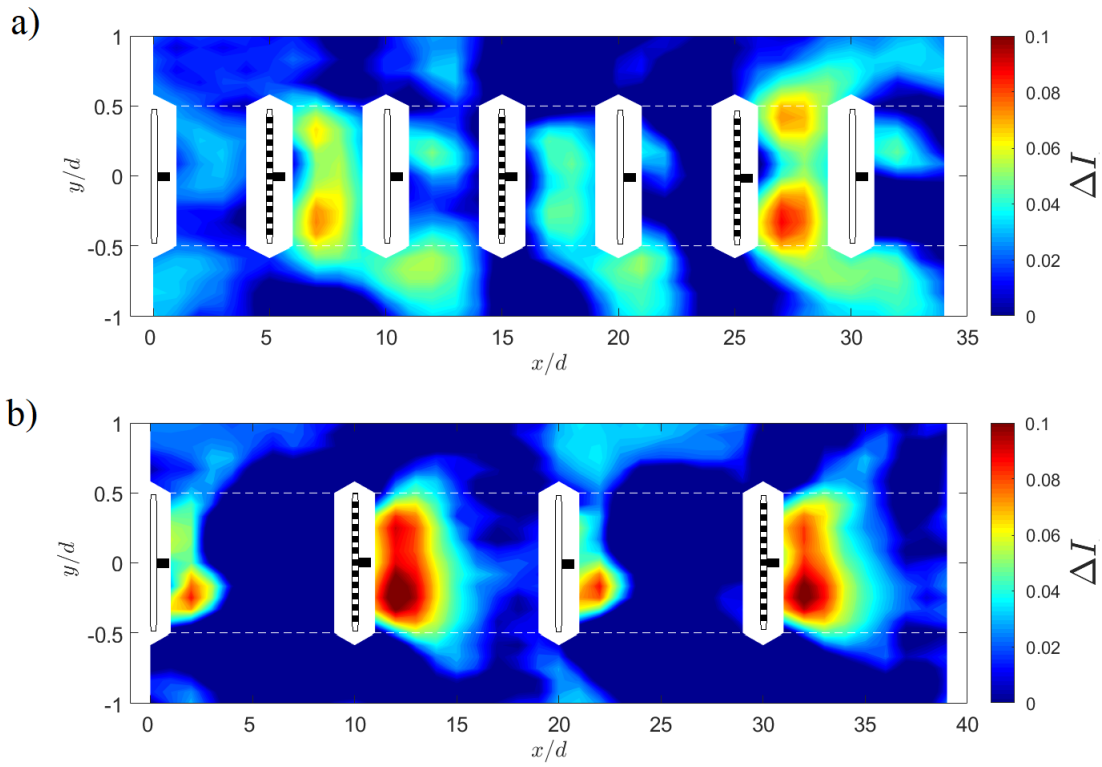

Figure A.4: Contours of turbulence intensity difference between two configurations (defined by Equation 4.2) in wall parallel plane at hub-height for a) $S_x = 5$; b) $S_x = 10$.

Appendix B

Supplementary results in central vertical plane

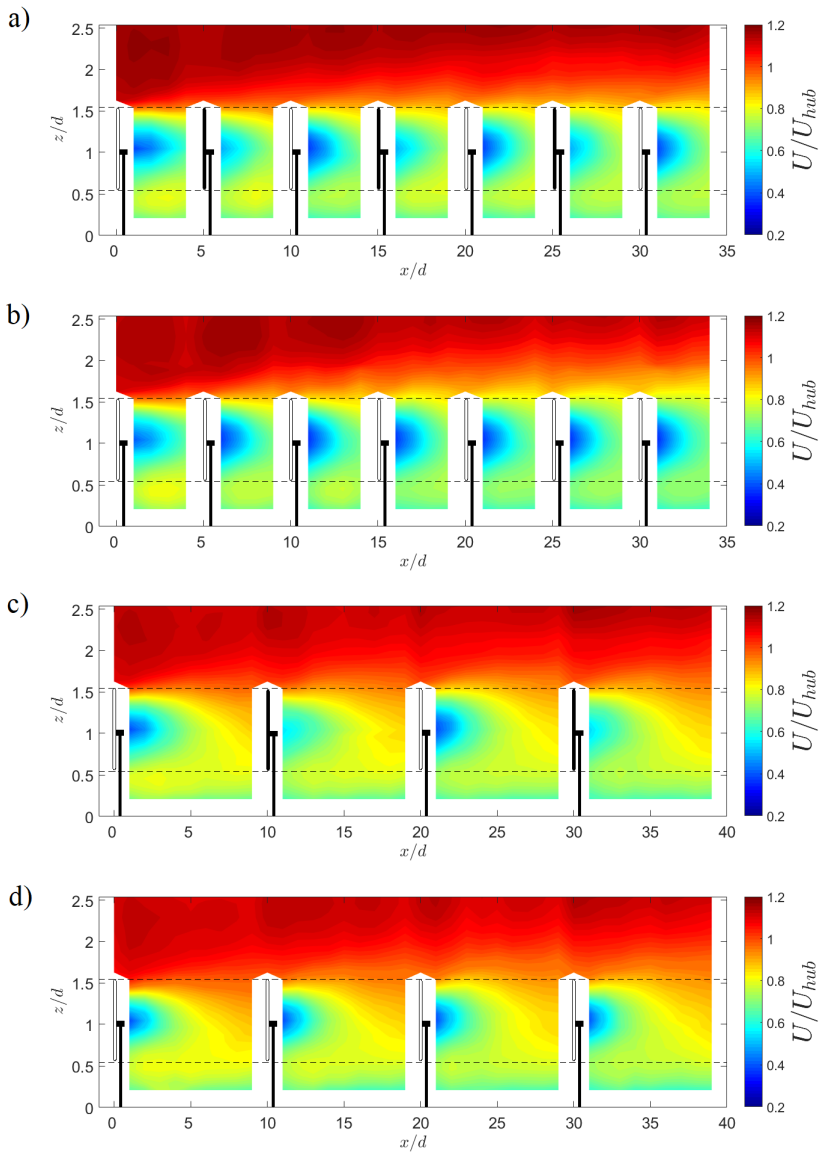

Figure B.1: Mean streamwise velocity contours in central vertical plane for a) configuration-A $S_x = 5$; b) configuration-B $S_x = 5$; c) configuration-A $S_x = 10$; d) configuration-B $S_x = 10$.

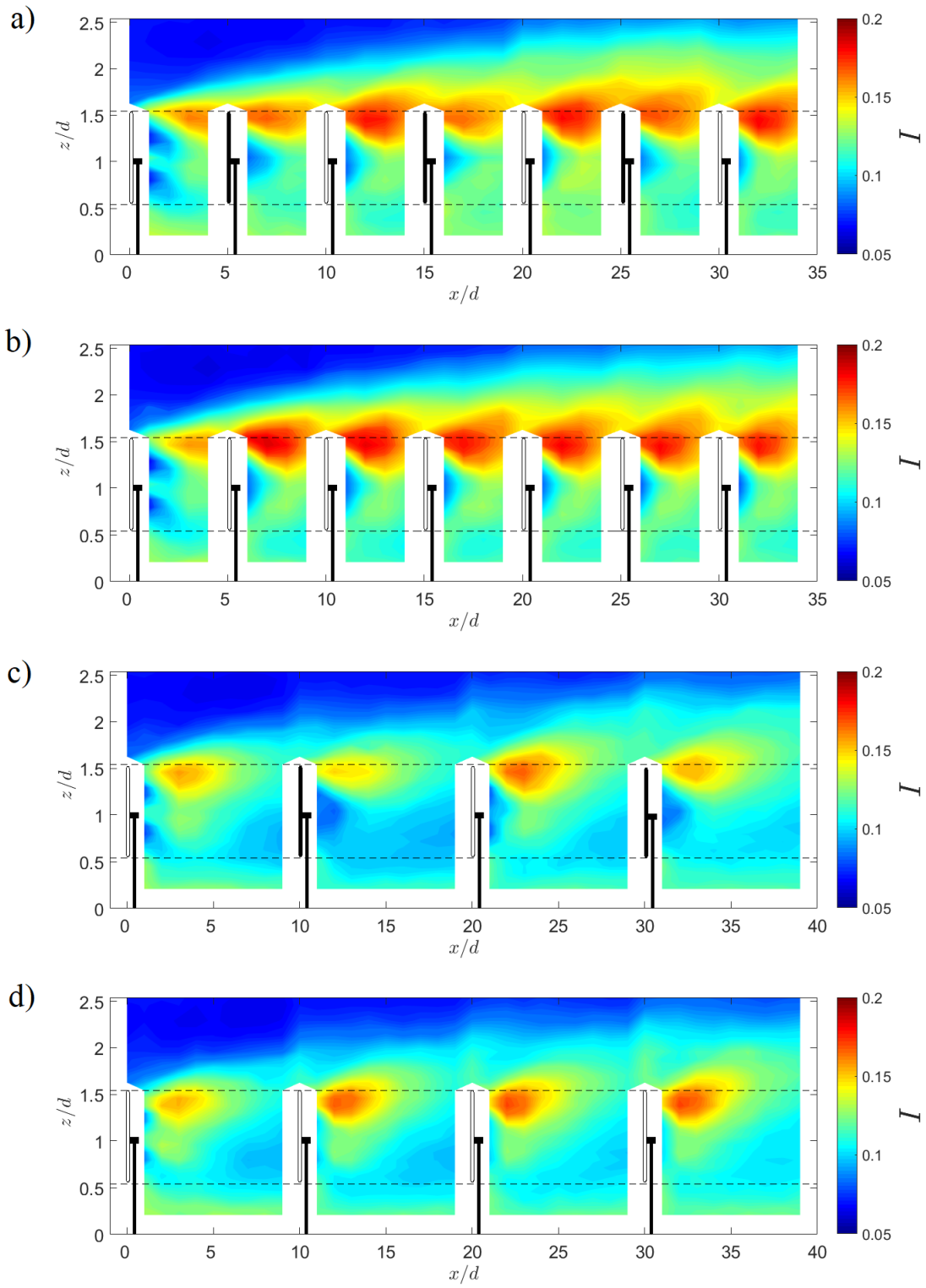

Figure B.2: Turbulence intensity contours in central vertical plane for a) configuration-A $S_x = 5$; b) configuration-B $S_x = 5$; c) configuration-A $S_x = 10$; d) configuration-B $S_x = 10$.

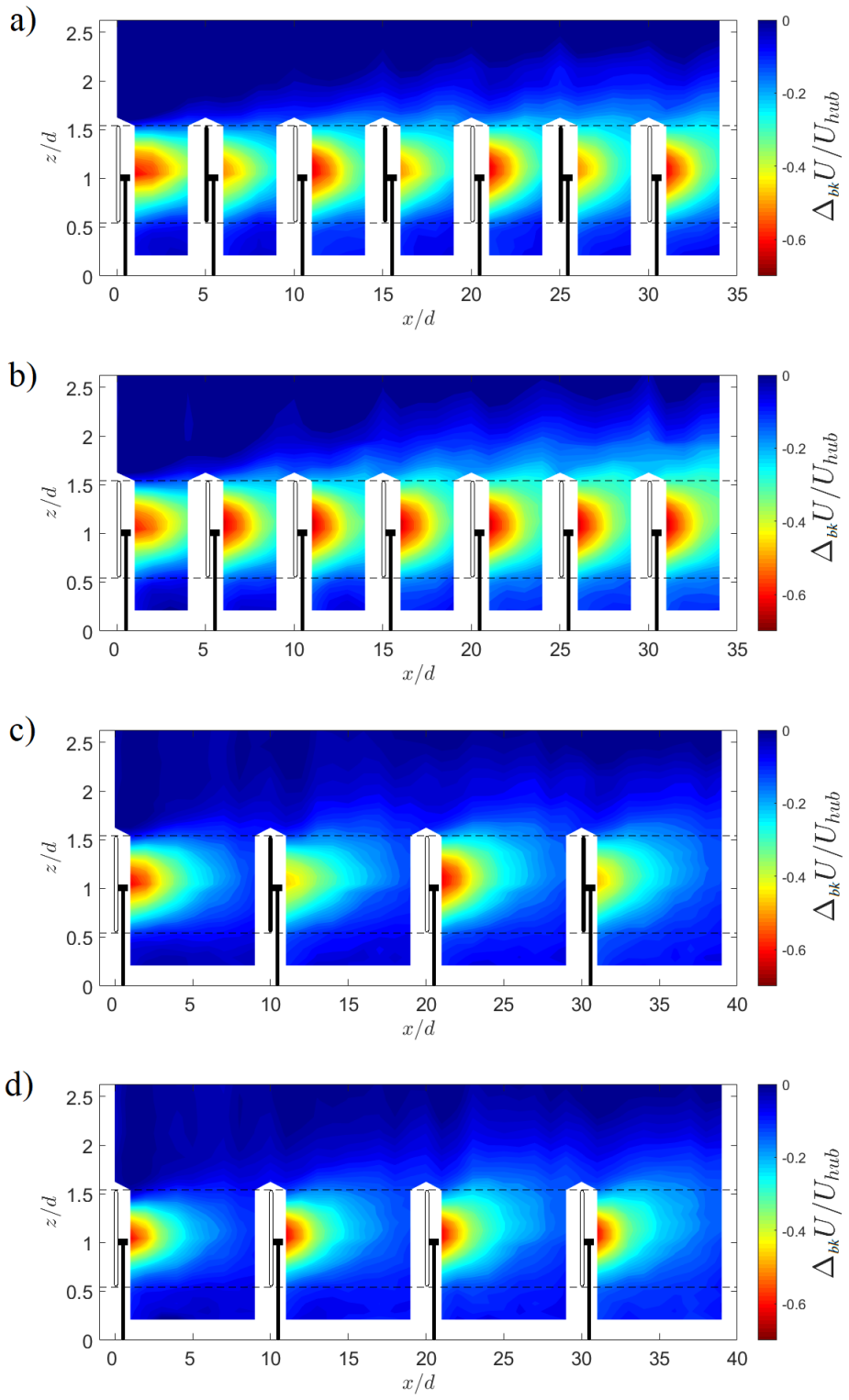

Figure B.3: Background flow filtered mean streamwise velocity ($\Delta_{bk}U = U - U_{bk}$) contours in central vertical plane for a) configuration-A $S_x = 5$; b) configuration-B $S_x = 5$; c) configuration-A $S_x = 10$; d) configuration-B $S_x = 10$.

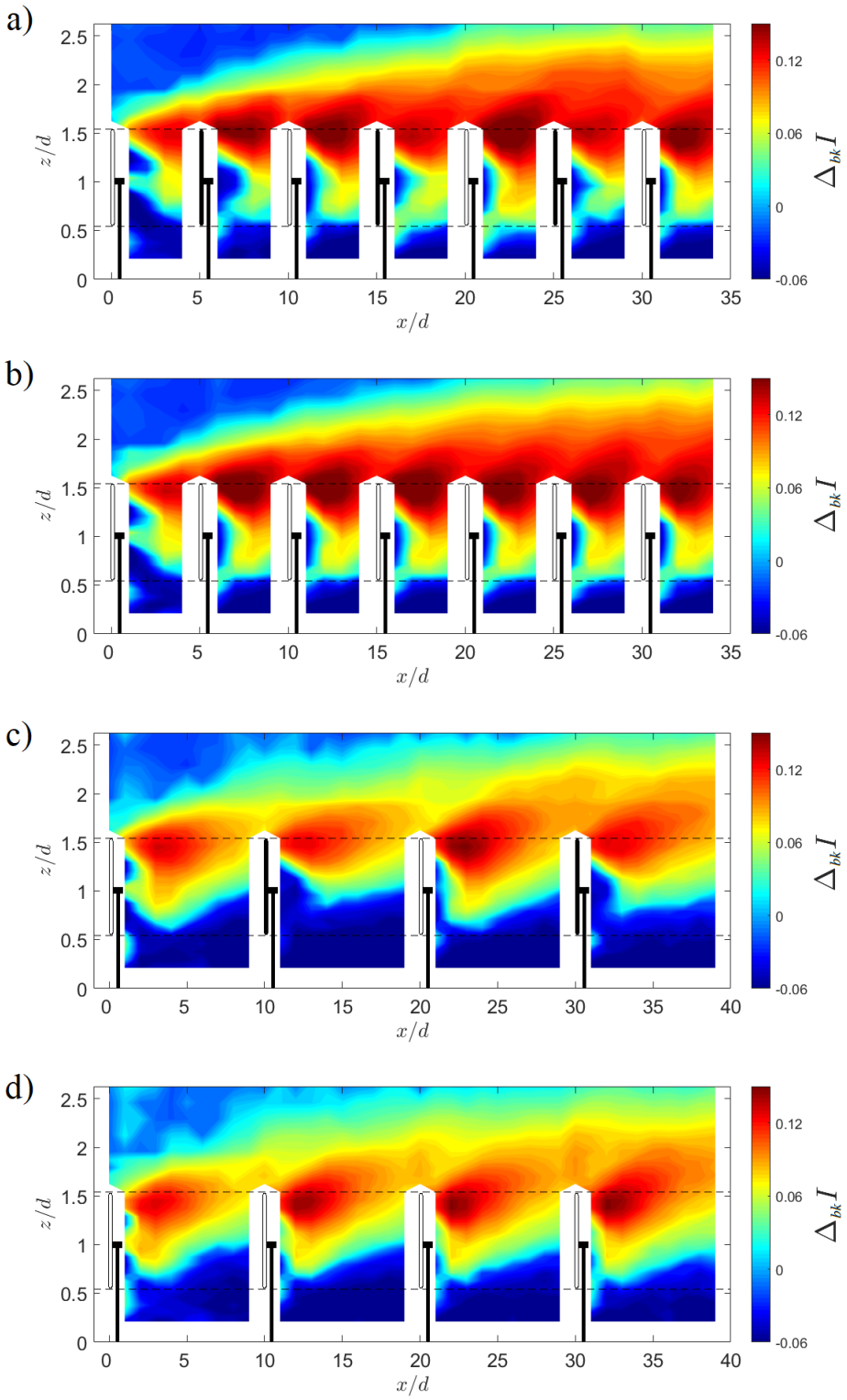

Figure B.4: Added turbulence intensity ($\Delta_{bk}I^2 = I^2 - I_{bk}^2$) contours in central vertical plane for a) configuration-A $S_x = 5$; b) configuration-B $S_x = 5$; c) configuration-A $S_x = 10$; d) configuration-B $S_x = 10$.